Title

Arp2/3 iso-complexes limit t-tubule overgrowth to ensure myofiber formation and synchronous contraction

Authors and affiliations

Ana Raquel Pereira*[1], Ana da Rosa Soares*[1], Tianyang Liu[2], Josie Liane Ferreira[2,3], Graciano Leal[1], Inês Faleiro[1], Naoko Kogata[4], Michael Way[4,5], Carolyn A. Moores[2], Edgar R. Gomes[1]

* these authors contributed equally to this work

[1] Instituto de Medicina Molecular, Faculdade de Medicina, Universidade de Lisboa, Avenida Professor Egas Moniz, 1649-028 Lisboa, Portugal

[2] Institute of Structural and Molecular Biology, Birkbeck College, London, WC1E 7HX, UK

[3] Institute of Structural and Molecular Biology, Division of Biosciences, University College London, London WC1E 6BT, UK

[4] Cellular signalling and cytoskeletal function laboratory, The Francis Crick Institute, 1 Midland Road, London, NW1 1AT, UK

[5] Department of Infectious Disease, Imperial College, London W2 1PG, UK

Summary

T-tubules are long plasma membrane invaginations that form contact sites with two adjacent endoplasmic reticulum compartments to generate a skeletal muscle triad. Although the importance of t-tubules is well established, and abnormalities are found in multiple muscle disorders, the mechanisms of t-tubule growth are currently unknown. We found that the branched actin nucleator Arp2/3 regulates t-tubule organisation in myofibers. Cortical actin limits t-tubule growth, suggesting that it must be locally disassembled to allow the t-tubule to grow. T-tubule overgrowth is limited by Arpc5-containing Arp2/3 iso-complexes, but not those containing Arpc5L. Loss of Arpc5 results in malformed t-tubule clusters, impaired triads, and asynchronous muscle contraction, as found in multiple muscle disorders. Therefore, limiting t-tubule overgrowth has a role in triad formation and myofiber contraction, providing a possible pathophysiological mechanism for these muscle disorders.

Graphical abstract

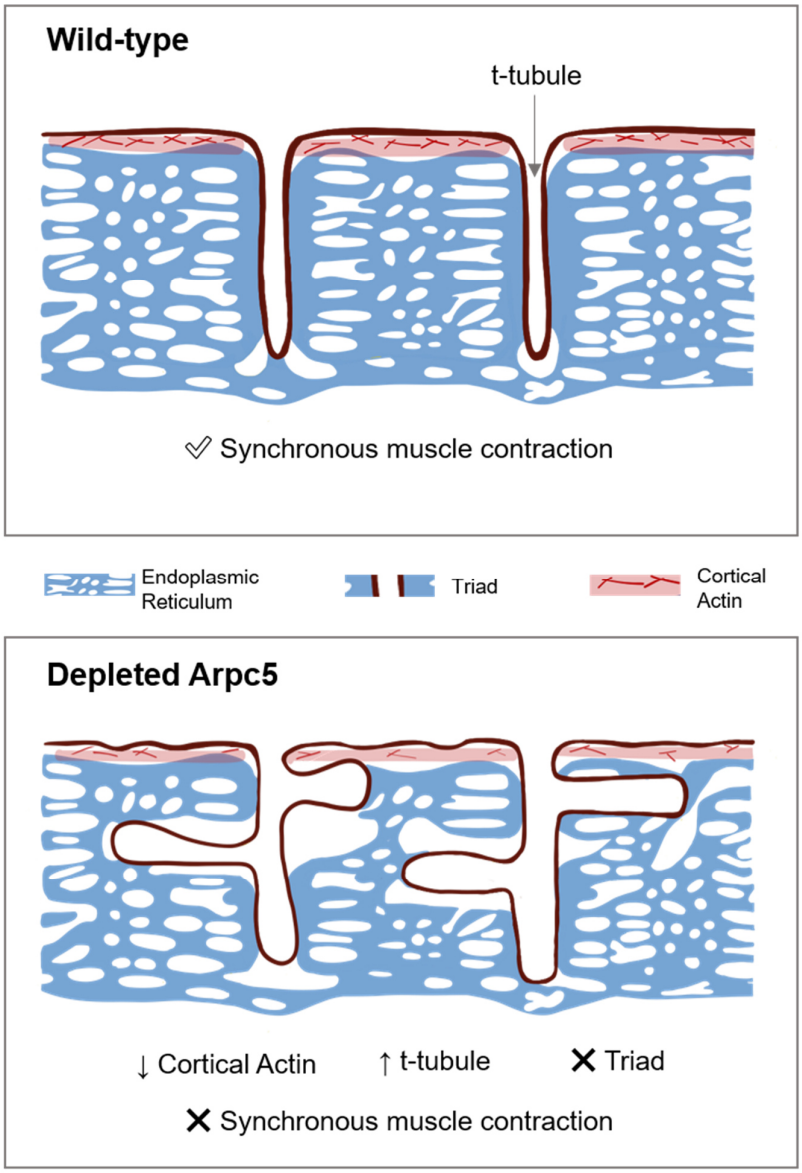

Keywords

Myofiber; Arp2/3 iso-complexes; Arpc5; cortical actin; t-tubule; muscle contraction

Introduction

The contractile properties of skeletal muscle and its connection to the skeleton are essential for body movement, posture, and breathing. These vital functions are affected by multiple disorders and decline with age. Sarcomeres are the contractile units of muscle cells and are organised in myofibril bundles. Myofibrils contract synchronously upon calcium release from the endoplasmic reticulum (ER), also known as sarcoplasmic reticulum, due to its specialisation in muscle cells. Muscle contraction is initiated at the neuromuscular junction by local depolarisation of the plasma membrane, which propagates throughout the muscle cell (myofiber) (Franzini-Armstrong, 2018). Since myofibers are the longest and thickest cells in the human body, the depolarisation signal must be transmitted throughout their entire volume (Ward et al., 2009). This is achieved by plasma membrane invaginations named transverse tubules (t-tubules) that surround myofibrils, and form membrane contact sites with two adjacent endoplasmic reticulum compartments, in a structure termed triad (Al-Qusairi and Laporte, 2011; Kawaguchi and Fujita, 2024; Porter and Palade, 1957). Depolarisation of the t-tubule membrane triggers calcium release from the ER, a phenomenon termed excitation-contraction coupling (EC-coupling). Disruptions in triad assembly and morphology result in EC-coupling abnormalities, characteristic of multiple muscle disorders (Dowling et al., 2014). While the structure and function of the mature triad are well-defined, the underlying mechanisms governing the biogenesis and remodelling of t-tubules and triads – processes that require extensive yet precisely targeted remodelling of muscle cell membranes - remain elusive.

During mammalian development, t-tubules emerge in the embryo, forming a tubular network and becoming transversely organised only after birth (Takekura et al., 2001). Recent observations suggest that t-tubule biogenesis is initiated from plasma membrane invaginations mediated by Bin1, a BAR domain-containing protein, and caveolin-3-containing caveolae (Lemerle et al., 2023). Caveolin-3 is then released from the t-tubules by Cavin4 to remodel the t-tubule network (Lo et al., 2021). Endosomal membrane traffic and stabilisation at the sarcomeres have been proposed and implicated in t-tubule network formation and maintenance (Al-Qusairi and Laporte, 2011; Hall et al., 2020). However, how t-tubules grow and how this growth impacts triad function is unknown.

Interactions between the plasma membrane and cortical actin are pivotal in membrane remodelling during fundamental cellular processes such as endocytosis and cell migration (Svitkina, 2020). The cortical actin cytoskeleton consists of both linear and branched actin filaments, the latter of which is nucleated by the Arp2/3 complex composed of 7 evolutionary conserved subunits (Campellone et al., 2023). Notably,

79 some Arp2/3 subunits are encoded by more than one gene in higher Eukaryotes, yielding
80 possibly eight unique Arp2/3 complexes in mammals with different properties (Abella et
81 al., 2016; Cao et al., 2024; Galloni et al., 2021; Pizarro-Cerdá et al., 2017). It has been
82 previously shown that this diversity in Arp2/3 iso-complexes is tailored for specific cellular
83 functions such as cell migration, viral transport, or T-cell activation (Abella et al., 2016;
84 Fäßler et al., 2023; Sadhu et al., 2023). In skeletal muscle, we previously demonstrated
85 that Arp2/3 complexes containing Arpc5L drive nuclei positioning to the periphery of
86 myofiber by promoting desmin-dependent myofibril crosslinking to generate centripetal
87 forces on the nucleus (Roman et al., 2017). We also showed that Arpc5 plays a crucial
88 role in triad organisation by an unknown mechanism.

89 Here we explored how Arpc5-containing iso-complexes are involved in triad
90 organisation. We found that t-tubules are dynamic, and Arpc5 and cortical actin limit t-
91 tubule overgrowth. Disruption of Arpc5, but not Arpc5L containing Arp2/3 complex,
92 results in defects in triad formation and asynchronous muscle contraction, as observed
93 in multiple muscle disorders.

Results

T-tubules are dynamic in mature and developing myofibers

To understand how the t-tubule network is established in myofibers, we first evaluated t-tubule dynamics. For this, we used matured myofibers isolated from adult mice or *in vitro* differentiating myofibers, incubated with a plasma membrane lipid dye (CellMask), which labels t-tubules, and performed time-lapse microscopy (Takekura et al., 2001). We observed that t-tubules exhibit growing and shrinking movements in both isolated myofibers (Figure 1A, Video S1) and developing myofibers (Figure 1B, Video S2). The mean growing speed of t-tubules in developing myofibers was 1.2 µm/sec (Figure 1B). T-tubules are known to establish membrane contact sites with the endoplasmic reticulum (ER), forming triads (Porter and Palade, 1957). Moreover, the ER of undifferentiated cells is highly dynamic (Lee and Chen, 1988; Nixon-Abell et al., 2016). We therefore wondered if the growing t-tubules were associated with ER or triad dynamics. We first looked at ER (GFP-KDEL) and t-tubule dynamics in differentiating myofibers. Although we observed that the ER of developing myofibers is dynamic, ER movement did not correlate with growing t-tubules and vice-versa (Figure 1C, Video S3). To address if t-tubules are dynamic at the triad, we imaged the movement of t-tubules and Triadin-GFP, an ER transmembrane protein that localises explicitly at triads (Sébastien et al., 2020). Triadin-GFP exhibits a negligible average speed of 0.015 µm/sec compared to the t-tubule growing average speed of 1.2 µm/sec (Figure 1D, Video S4). Additionally, in 100% of growing t-tubules, we did not observe Triadin-GFP moving with the t-tubule (N=39). These results indicate that t-tubules grow in developing and fully matured myofibers, and this growth is independent of ER and triad dynamics.

Inhibition of the Arp2/3 complex promotes t-tubule growth

Our previous results reported that triad organisation during myofiber formation depends on the Arp2/3 complex (Roman et al., 2017). Building upon these initial observations, we hypothesise that the Arp2/3 complex is required for t-tubule growth. To this end, we established a cellular system to study t-tubule dynamics. For this purpose, we generated a stable cell line of C2C12 myoblasts expressing GFP-Bin1 (GFP-Bin1 myoblasts) since expression of Bin1 is sufficient to induce t-tubules, as previously reported (Video S5) (Lee et al., 2002). We treated GFP-Bin1 myoblasts with the Arp2/3 inhibitor CK-666, and contrary to our hypothesis, we observed a significant increase in the number of growing t-tubules after CK666 treatment (Figure 2A; Video S5 and S6). This effect was not only observed in GFP-Bin1 myoblasts since treatment of developing

129 myofibers with CK666 also increased the number of growing t-tubules (Figure 2B; Video
130 S7 and S8). Together, these results show that Arp2/3 inhibition promotes t-tubule
131 overgrowth.

132 We previously showed that the Arp2/3 complex containing Arpc5, but not its
133 isoform Arpc5L, is involved in triad organisation (Roman et al., 2017). To test if Arpc5
134 and Arpc5L had differential roles on t-tubule growth, we performed knock-down (KD)
135 experiments with siRNA targeting either Arpc5 or Arpc5L in GFP-Bin1 myoblasts or
136 developing myofibers (Figure S1). Quantification of the number of growing t-tubules
137 revealed that depletion of Arpc5, but not Arpc5L, results in significantly more growing t-
138 tubules than control in both GFP-Bin1 myoblasts and in developing myofibers (Figure
139 2C and 2D; Video S9-S14). Overall, these results suggest that Arp2/3 complexes
140 containing the Arpc5 but not the Arpc5L limit t-tubule growth.

141

142 **F-Actin does not accumulate near growing t-tubules**

143 It has been previously shown that actin cytoskeleton and Arp2/3 can modulate
144 membrane tubulation in multiple organelles (Allard et al., 2021). Since our results
145 suggest that the Arp2/3 complex has a role in limiting t-tubule growth, we next wondered
146 if there was actin enrichment at the growing t-tubules. To this end, we imaged actin
147 filaments (F-actin) using either LifeAct-mCherry or mScarlet-Utrophin reporters in GFP-
148 Bin1 myoblasts (Figure 3A and 3C). As expected, we observed F-actin throughout the
149 cytoplasm, forming actin bundles (actin cables or stress fibers), filopodia, and
150 lamellipodia, and enriched around some intracellular vesicles (Video S15 and S16). To
151 quantify actin dynamics in the vicinity of growing t-tubules, we measured the average
152 intensity of F-actin fluorescence at a small ROI close to the growing t-tubule over time.
153 We did not observe F-actin enrichment during t-tubule growth, suggesting that F-actin is
154 not nucleated near growing t-tubules (Figure 3B and 3D; Video S15 and S16). To further
155 investigate the organisation of F-actin close to t-tubules, we performed cryo-correlative
156 Light and Electron Microscopy (cryo-CLEM) and cryo-electron tomography (cryo-ET) of
157 GFP-Bin1 myoblasts in regions containing t-tubules (Figure S2, 3E-G). We observed
158 unbranched F-actin forming bundles or meshes throughout the different volumes (Figure
159 3H, S3A and S3B, Video S17-S19). However, when we analysed slices of the volume at
160 different z positions, no distinct arrangement of actin filaments was observed near the t-
161 tubules when compared to other cytoplasmic regions (Figure 3I, S3C-J). Importantly, we
162 observed very few actin branches around t-tubules (Figure 3I), and we did not observe
163 more branched actin close to the t-tubules when compared to other regions of the

164 cytoplasm (Figure S3C-J, compare branched actin in blue versus red ROI). This
165 contrasts to what is observed for clathrin-mediated endocytosis, where branched actin
166 is enriched near the endocytic membrane (Collins et al., 2011; Serwas et al., 2022).
167 Overall, these data suggest that branched F-actin does not accumulate near growing t-
168 tubules, leading us to explore contributions by the Arp2/3 network to t-tubule dynamics
169 elsewhere in the cell.

170 **Perturbation of cortical actin promotes t-tubule growth**

171 T-tubules are contiguous with the plasma membrane, and the t-tubule surface area
172 is about seven times the myofiber surface area (Peachey, 1965). This suggests that
173 during development, a large amount of membrane must be available to invaginate and
174 form t-tubules. Plasma membrane morphology is regulated by cortical actin, the major
175 component of the cell cortex that forms an actomyosin network underneath the plasma
176 membrane (Chugh and Paluch, 2018; Svitkina, 2020). Since the Arp2/3 complex is also
177 involved in cortical actin remodelling, we hypothesised that perturbing cortical actin
178 impacts t-tubule growth (Bovellan et al., 2014). To test this hypothesis, we interfered with
179 cortical actin by inhibiting non-muscle myosin-2, using para-aminoblebbistatin
180 (blebbistatin), and quantified the number of growing t-tubules before and after treatment
181 (Laplaud et al., 2021; Várkuti et al., 2016). We found that both in GFP-Bin1 myoblasts
182 and in developing myofibers, blebbistatin treatment led to a significant increase in the
183 number of growing t-tubules (Figure 4A and 4B; Video S20-23). We also interfered with
184 cortical actin by inducing a glycerol hyperosmotic shock, which leads to a rapid
185 remodelling of cortical actin due to a reduction of cell volume (Di Ciano et al., 2002). We
186 quantified the number of growing t-tubules before and after osmotic shock in both
187 myoblasts (Figure 4C; Video S24 and S25) and developing myofibers (Figure 4D; Video
188 S26 and S27), and observed a significant increase in the number of growing t-tubules
189 upon osmotic shock. These results show that perturbations of the cortical actomyosin
190 network promote t-tubule growth, suggesting that cortical actin limits t-tubule growth.

191

192 **Arpc5 depletion leads to t-tubule clusters and impaired triad formation**

193 Our data are consistent with a model in which Arp2/3 complexes containing Arpc5
194 mediate cortical actin, limiting t-tubule growth. In fully differentiated myofibers, t-tubules
195 establish two-sided connections with the ER, forming triads that become transversely
196 organised (Al-Qusairi and Laporte, 2011; Kawaguchi and Fujita, 2024; Porter and
197 Palade, 1957). Since Arpc5, but not Arpc5L is involved in transverse triad organisation
198 (Roman et al., 2017), we investigated the role of Arpc5 isoforms in the t-tubule network

199 of fully differentiated myofibers. To this end, we assessed t-tubule transverse alignment
200 in myofibers depleted for either Arpc5 or Arpc5L in fully differentiated myofibers, which
201 have transverse triads (Falcone et al., 2014; Roman et al., 2017). In control and Arpc5L
202 KD conditions, we observed transversely aligned t-tubules forming an evenly distributed
203 network throughout the myofiber (Figure 5A, Scramble and si Arpc5L). However, in
204 Arpc5 KD myofibers, we observed that t-tubules were not transversely aligned, and t-
205 tubules formed clusters (Figure 5A and 5C). T-tubule clusters were not an artefact of
206 CellMask as they were also observed upon immunostaining against Bin1, a t-tubule-
207 specific protein (Figure 5B). To better characterise t-tubule clusters, we performed
208 transmission electron microscopy (TEM) of stained and resin-embedded differentiated
209 myofibers. We observed a higher proportion of enlarged t-tubules in Arpc5 KD myofibers
210 when compared to the control (Figure S4A yellow arrows, S4B). Additionally, we noticed
211 that these enlarged t-tubules still form contact sites with the ER (Figure S4A blue arrows)
212 but only with one ER compartment. Accordingly, we observed a reduction of triads in
213 Arpc5 KD compared to the control (Figure S4A green arrows, S4C). Finally, we
214 quantified the number of Junctophilin-1 (JPH1) puncta, a marker of triads, in fully
215 differentiated myofibers and observed that Arpc5 KD myofibers, but not Arpc5L or
216 control, exhibited a reduced number of JPH1 puncta, suggesting impaired triad formation
217 (Figure 5D and 5E). Together, these results show that lack of Arpc5, which induces t-
218 tubule overgrowth, contributes to disruption of the t-tubule network, leading to abnormal
219 t-tubule-ER contact sites and triad impairment.
220

221 **Arpc5 is required for synchronous excitation-contraction coupling**

222 Triads are fundamental for coupling the excitation of the plasma membrane and t-
223 tubules to the release of calcium from the ER into the cytosol, resulting in muscle
224 contraction. This process is known as excitation-contraction coupling (EC-coupling).
225 Since we observed that Arpc5 depletion induces t-tubule clusters and impaired triads,
226 we assessed the impact of the loss of Arpc5 on EC-coupling in myofibers. We first
227 measured cytosolic calcium levels upon electrical pulses by imaging differentiated
228 myofibers infected with an AAV expressing the calcium reporter GCaMP (Chen et al.,
229 2013). As expected in the controls, we observed GCaMP fluorescence transients
230 corresponding to calcium release and uptake from the ER, synchronised with electrical
231 stimulation (Figure 6A and 6B, scramble). In contrast, most myofibers depleted for Arpc5,
232 but not Arpc5L exhibited abnormalities in calcium transients, which were not
233 synchronised with the electrical stimulation pulses (Figure 6A and 6B). We then
234 investigated whether this asynchrony between excitation and calcium transients impairs

235 contraction. For this purpose, we performed single-myofiber contraction tracing and
236 found that myofibers could still contract when Arpc5 and Arpc5L are depleted, as in the
237 scramble control (Figure 6C and 6D). However, there was a dramatic asynchrony
238 between electrical stimulation and myofiber contraction in the Arpc5 KD myofibers but
239 not in the Arpc5L and scramble conditions (Figure 6C and 6E). This observation
240 suggests that lack of Arpc5 results in defects in EC-coupling that leads to asynchronous
241 muscle contraction, highlighting the role of Arpc5 containing Arp2/3 complexes and t-
242 tubule overgrowth in triad function.
243

Discussion

T-tubules and their connection with the endoplasmic reticulum to form triads are fundamental to muscle contraction and are disrupted in multiple muscle disorders. We found that t-tubules are dynamic, and Arpc5-containing Arp2/3 iso-complexes limit their growth through the modulation of cortical actomyosin. T-tubule overgrowth upon disruption of Arpc5, but not Arpc5L, results in t-tubule clusters, impaired triads, and asynchronous muscle contraction, thus providing a pathophysiological mechanism for muscle disorders with impaired triad function (Dowling et al., 2014).

Keith Porter and George Palade originally identified triads, which were the first description of a plasma membrane contact site (Porter and Palade, 1957). We found that t-tubules are dynamic, even in matured myofibers isolated from adult mice, although to a lesser extent than in developing myofibers. T-tubule dynamics are independent of ER dynamics and triads, which further supports that ER organisation precedes t-tubule network formation, as observed during muscle development (Flucher et al., 1993). T-tubule dynamics in matured myofibers may be involved in triad homeostasis and repair during muscle injury.

Since the t-tubule area comprises up to seven times more of the myofiber cell membrane, considerable membrane remodelling is required to form a t-tubule network during development (Peachey, 1965). Our results suggest that cortical actin prevents t-tubule overgrowth since perturbation of cortical actin through non-muscle myosin-2 inhibition, hyperosmotic shock, and Arp2/3 complex inhibition lead to more growing t-tubules. Therefore, we hypothesise that to grow a t-tubule, cortical actin must be disassembled to allow plasma membrane release and availability for the t-tubule to grow. Upon stretch release of adherent cells, tubulation of the plasma membrane has also been observed, suggesting that membrane release facilitates tubulation, although the role of cortical actin has not been addressed (Kosmalska et al., 2015). The formation of tubules from membranes directly depends on membrane release as elegantly demonstrated using giant lipid vesicles. Excess membrane area created by a decrease in vesicle volume leads to membrane release and tubulation towards the lumen of the vesicle, similar to t-tubule growth (Li et al., 2011). In myofibers, disruption of cortical actin probably results in the excess plasma membrane required for t-tubule growth. Furthermore, the observed tubulation in lipid vesicles does not involve any external forces (Li et al., 2011). In myofibers, during t-tubule growth, we did not detect any enrichment of actin, using multiple F-actin fluorescent probes. Using cryo-CLEM, we also did not observe evidence for interaction between F-actin and t-tubules, nor accumulation of branched actin. Although we cannot rule out that external forces are involved in t-tubule growth, our data does not support a need for actin-related force generation.

281 Although tubulation can occur in the absence of proteins in lipid vesicles upon a decrease
282 in membrane volume, Bin1 modulates membrane tubulation in the absence of actin
283 without a reduction of membrane volume (Picas et al., 2014). Bin1, together with other
284 proteins such as dynamin-2, are therefore of importance for t-tubule network
285 remodelling, probably providing the required forces to maintain tubulation, together with
286 the cortical actin membrane release mechanism we describe here (Lionello et al., 2022;
287 Picas et al., 2014).

288 Branched cortical actin is nucleated by the Arp2/3 complex at the cell cortex and is
289 crosslinked by non-muscle myosin-2 to generate cortical tension essential for plasma
290 membrane remodelling and cell shape (Chugh and Paluch, 2018; Svitkina, 2020).
291 Downregulation of the Arp2/3 complex reduces cortical actin and weakens the coupling
292 of the plasma membrane with the cell cortex (Bovellan et al., 2014). Our results suggest
293 that Arp2/3 iso-complexes containing Arpc5 or Arpc5L might regulate cortical actin in a
294 specific manner. However a role for a specific Arp2/3 isocomplex on cortical actin has
295 yet to be described. During lamellipodia formation, Arp2/3 iso-complexes containing
296 Arpc5 or Arpc5L have a distinct role in actin network architecture and branched actin
297 structure modulation (Fäßler et al., 2023). We speculate that similar distinct actin network
298 arrangements might occur at the cell cortex to limit t-tubule formation through Arpc5 but
299 not Arpc5L containing Arp2/3 complexes.

300 Our work implicates a role in limiting t-tubule dynamics for effective triad function
301 and synchronous contraction. T-tubule overgrowth might result in defects on membrane
302 contacts with the ER, impairing the formation and maintenance of functional triads.
303 Interfering with the t-tubule network by depletion of Cavin4 also leads to t-tubule cluster
304 accumulation and disruption of triads (Lo et al., 2021). Also, t-tubule overgrowth and triad
305 abnormalities have been described in aged human muscle (Boncompagni et al., 2006).
306 Furthermore, several muscle disorders with impaired triads also exhibit an overgrowth
307 of t-tubule clusters, particularly in Mitsugummin25, Dysferlin, Myotubularin, or Dynamin-
308 2 mutants (Al-Qusairi and Laporte, 2011; Dowling et al., 2014). Therefore, modulation of
309 t-tubule growth and cluster formation can be a common target to ameliorate or prevent
310 these diseases.

311

312 ## Methods

313 ### T-tubule labelling in matured myofibers

314 All procedures using animals were approved by the Institutional Ethics Committee and
315 followed the guidelines of the Portuguese National Research Council Guide (DGAV). Ex
316 vivo isolated single myofibers from Extensor Digitorum Longus (EDL) muscles were
317 generated using the protocol previously described (Falcone et al., 2014). EDL muscle
318 was explanted from 8- to 12-week-old male or female C57BL/6J mice and then digested
319 in DMEM (Invitrogen) containing 0.2% type I collagenase (Sigma) for 2 h at 37°C.
320 Mechanical dissociation of fibers was performed using a thin Pasteur pipette in a
321 transilluminating-fluorescent stereomicroscope. Single fibers were collected and plated
322 in ibidi-35mm-dishes pre-coated with 1% matrigel in Iscove's Modified Dulbecco's Media
323 (IMDM, Invitrogen) with Glutamax. After plating, cells were covered with an upper coating
324 of ice-cold 50% matrigel coating in IMDM with Glutamax. Plated myofibers were
325 maintained in 10% horse serum (Fisher Scientific) plus IMDM with Glutamax for the
326 duration of the experiment. To visualize t-tubule dynamics, plated myofibers were
327 labelled for 30 minutes with CellMask Orange (1 µM, Invitrogen).

328

329 ### In vitro myofibers

330 All animal procedures were approved by the institutional ethics committee and followed
331 the guidelines of the National Research Council Guide for the care and use of laboratory
332 animals. In vitro myofibers were differentiated as previously described (Pimentel et al.,
333 2017) from primary myoblasts isolated from 5 to 7-day-old mixed-gender C57BL/6 mice.
334 Tibialis anterior (TA), EDL, Gastrocnemius and Quadriceps muscles were dissected and
335 kept in ice-cold PBS. Muscles were digested mechanically using surgical scissors and
336 incubated for 90 min at 37ºC with agitation in collagenase type V (Sigma) and dispase II
337 (Roche) in DPBS. The digestion was stopped by mixing 10% FBS 1% Penicillin-
338 Streptomycin IMDM with Glutamax. The cells suspension was centrifuged for 5 min at
339 75 x g to remove debris followed by a second centrifugation for 5 min at 350 x g. After
340 centrifugation, cells were resuspended in the same medium and pre-plated for 4 hours
341 to allow for fibroblasts adherence. The cells remaining in suspension were collected,
342 centrifuged for 5 min at 350 x g and plated at a density of 220 000 cells/ml in 20% FBS
343 IMDM with Glutamax in ibidi 35 mm dishes pre-coated with 1% matrigel in IMDM with
344 Glutamax. After three days of proliferation, medium was replaced by 10% horse serum
345 IMDM with Glutamax supplemented with 100 ng/ml recombinant agrin to induce

346 differentiation. An ice-cold upper coating of 50% matrigel in 10% horse serum IMDM with
347 Glutamax was added the following day and fresh medium was added. Experiments were
348 performed either at 4-5 or 7-8 days after differentiation.

349

350 **siRNAs, plasmids and transfections**

351 Triadin-GFP (Trisk95-GFP, (Fourest-Lieuvin et al., 2012)) or GFP-KDEL (Campbell-
352 Valois et al., 2012) plasmids were transfected on in vitro myofibers three days after
353 plating with 1 µg of DNA per ibidi-35mm-dish of the appropriate plasmid using
354 Lipofectamine 2000 (Thermo), according to manufacturer's protocol.

355 GFP-Bin1 myoblasts were transfected with 1 ug plasmid/ibidi-35mm-dish of LifeAct-
356 mCherry (Janota et al., 2022) or mScarlet-I-UtrCH (gift from Dorus Gadella, Addgene
357 plasmid #98823; http://n2t.net/addgene:98823; RRID:Addgene_98823 (Chertkova et al.,
358 2017)) one day after plating, using Lipofectamine 2000 (Thermo), according to
359 manufacturer's protocol. Cells were imaged by vtiSIM microscope on the next day (see
360 below).

361 For Arpc5 isoforms depletion, in vitro myofibers were transfected with Thermo Fisher
362 Silencer® Select siRNAs for Arpc5 (ID#s85623) and Arpc5L (ID#s211945), 3 days after
363 plating with 20nM/ibidi-35mm-dish of the appropriate siRNA using Lipofectamine
364 RNAiMAX. Silencer® Select Scramble(ID #4390843) was used as a negative control.

365

366 **Generating the GFP-Bin1 myoblast stable cell line**

367 GFP-Bin1 stable cell line of C2C12 myoblasts (GFP-Bin1 myoblasts) was generated
368 using a pLVX-puromycin vector containing Bin1. The lentiviral vector was constructed
369 with VectorBuilder. The vector ID is VB220728-1365nbr, which can be used to retrieve
370 detailed information about the vector on vectorbuilder.com. Lentivirus were produced in
371 HEK 293T cells. To generate stable cell lines expressing exogenous GFP-Bin1, C2C12
372 myoblasts were plated in a 6-well plate. The cells with a 10% confluency were carefully
373 covered with 0.5 ml of filtered medium containing the lentiviruses and 0.5 ml of complete
374 medium was added to myoblasts (1 ml total volume). The medium containing lentiviruses
375 was left over day, then 1 ml of complete fresh medium was added. Cells were allowed
376 to grow until 80% of confluency. Subsequently, the sorted myoblasts were allowed to
377 expand, and the process was repeated for three rounds of sorting to achieve a
378 homogeneous cell population.

379 GFP-Bin1 myoblasts were cultured in Dulbecco's modified Eagle's medium (DMEM) with
380 glutamine (Gibco) supplemented with 10% fetal bovine serum (FBS; Gibco) and
381 penicillin-streptomycin (100 U/ml:100 µg/ml; Gibco), at 37°C under 5% CO_2.

382

383 **Fluorescence microscopy**

384 Airyscan images were acquired using a Zeiss LSM980 Airyscan2 microscope, equipped
385 with a 63x Plan-Apochromat DIC oil objective (NA 1.4). Imaging was performed at 37°C
386 with 5% of CO_2 using the ZEN 3.8 blue edition. To measure t-tubule growth, images
387 were recorded every three seconds. Airyscan reconstruction was performed using
388 automatic filter settings.

389 For instant structured illumination microscopy (iSIM) imaging, the vtiSIM module
390 (Visitech) equipped on a Nikon Tie microscope with a 100x AC Oil CFI SR HP Apo TIRF
391 objective, and a Photometrics Prime BSI Express Scientific sCMOS camera was used.
392 Timelapse imaging was performed at 37°C with 5% of CO_2.

393 To visualize t-tubule dynamics in myofibers, the membrane lipid dye CellMask Orange
394 (1 µM, Invitrogen) was added to the myofibers 5-10 min before imaging. T-tubule and/or
395 ER dynamics were recorded by timelapse imaging using Airyscan microscopy (see
396 above).

397 To visualize actin dynamics in the vicinity of growing t-tubules, GFP-Bin1 myoblasts
398 transfected with LifeAct-mCherry or mScarlet-I-UtrCH were imaged by vtiSIM timelapse
399 imaging every second for three minutes.

400 To visualize t-tubule network and t-tubule clusters, developed in vitro myofibers
401 (differentiation day 7) were incubated with 1 µM of CellMask Deep red (Invitrogen).
402 Spinning disk confocal imaging was performed using a Zeiss Axio Observer microscope
403 equipped with a Yokogawa CSU-X1 scanning unit, an Evolve 512 EMCCD camera and
404 a 63x Plan-Apochromat DIC oil objective (N.A. 1.4), using the ZEN 3.2 blue edition
405 software. Cells were kept at 37°C and 5% of CO_2. Myofibers with more than three t-
406 tubule clusters were visually quantified using Fiji software and the percentage of cells
407 with t-tubule clusters was plotted using graphpad.

408

409

410

411 **Drug treatments**

412 Cells were treated with 100 µM of CK666 (Sigma) for Arp2/3 inhibition. A final
413 concentration of 125 µM of para-aminoblebbistatin (Motorpharma) was used to block
414 myosin-II. The number of growing t-tubules was performed immediately after drug
415 treatments for GFP-Bin1 myoblasts and after five minutes for myofibers. T-tubule
416 dynamics were recorded by timelapse imaging using Airyscan microscopy. GFP-Bin1
417 myoblasts treated with para-aminoblebbistatin were recorded by timelapse imaging
418 using vtiSIM microscopy.

419

420 **Glycerol treatment**

421 Myoblasts and developing myofibers were exposed to 225 mM and 45 mM of glycerol,
422 respectively, to induce hyperosmotic shock. The number of growing t-tubules was
423 performed three minutes after glycerol treatment for GFP-Bin1 myoblasts and after five
424 minutes for myofibers. Myofiber t-tubule dynamics were recorded by timelapse imaging
425 using Airyscan microscopy. GFP-Bin1 myoblasts t-tubule dynamics were recorded by
426 timelapse imaging using vtiSIM microscopy.

427

428 **Immunostaining**

429 Developed myofibers (differentiation day 7) were fixed in 4% paraformaldehyde in PBS
430 for 10 minutes at room temperature and permeabilized with 0.5% Triton X-100 for 5
431 minutes. Cells were blocked in a solution containing 10% goat serum, 5% BSA and
432 VisUBlock Mouse on Mouse Blocking Reagent (R&D Systems, VB001). Primary and
433 secondary antibodies were diluted in 0.1% saponin. Cells were incubated with primary
434 antibodies overnight at 4°C and washed three times for 10 minutes with PBS. Cells were
435 incubated with secondary antibodies for 1 hour at room temperature and washed three
436 times for 10 minutes with PBS. Cells were mounted with Fluoromount-G (Invitrogen).
437 Antibodies used for immunostaining were: anti-JPH1 Antibody (1:200 dilution,
438 Invitrogen, 40-5100); and anti-rabbit Alexa Fluor 488 secondary antibody (1:400, Life
439 Technologies). Phalloidin conjugated with an Alexa Fluor 647 A22287(1:200, Life
440 Technologies) was used to stain filamentous actin. Myofibers were imaged using the
441 vtiSIM microscope.

442

443

444

445 **Image analysis**

446 All images were processed in Fiji (Schindelin et al., 2012). For cell drift correction we
447 used the Fiji plugin Fast4Dreg (Pylvänäinen et al., 2023).

448 For t-tubule growth speed measurements, manual tracking of the tip of the t-tubule during
449 the timelapse was performed using Fiji manual tracking.

450 The number of growing t-tubules was manually recorded using the Fiji cell counter tool.
451 This value was then normalized for the cell area. All quantifications were performed
452 within two-minute timelapses.

453 To measure Triadin-GFP mean speed in developing myofibers, we used Airyscan
454 images of Triadin-GFP timelapses acquired every three seconds for two minutes. Since
455 Triadin-GFP localizes as distinct spots, we used the Fiji plugin Trackmate (Ershov et al.,
456 2022) to track Triadin-GFP spots over time in myofibers. To detect Triadin-GFP spots
457 we used the LoG detector with an estimated object diameter of 0.5 µm and a quality
458 threshold of 5, 10 or 20. We then linked the spots to generate tracks, by using the LAP
459 tracker with a max distance of 0.5 µm and no gap closing. To have enough datapoints
460 to calculate speed trajectories, we only considered tracks that lasted more than 10
461 frames (30 seconds). The resulting tracked Triadin-GFP spots were then used to
462 calculate mean speed.

463 To quantify actin dynamics in the vicinity of growing t-tubules, we manually selected a
464 ROI around GFP-Bin1 growing t-tubules (as the ones represented in Figure 2A and 2C),
465 including a few timepoints before the GFP-Bin1 signal was observed using Fiji software.
466 We then extracted at each timepoint the average of fluorescence intensity per μm^2 for
467 GFP-Bin1, LifeAct-mcherry or mScarlet-I-UtrCH using the Fiji software. Values were
468 normalized for the initial corresponding average intensity value and these normalized
469 intensity values per μm^2 over time were plotted using graphpad.

470 To automatically count the number of Junctophilin 1 (JPH1) puncta, a maximum
471 projection of the Z-stack images that were in focus was first performed using Fiji. Then,
472 a rectangular ROI with an area of 175.552 μm^2 was drawn along the myofiber length. To
473 detect the puncta automatically, we used the LoG detector tool from the FIJI TrackMate
474 plugin (Schindelin et al., 2012) LoG filters for puncta detection were a blob diameter of
475 0.5 µm and an intensity threshold of 5. To analyse the number of JPH1 puncta per μm^2,
476 the number of detected puncta was normalized for ROI area and plotted.

477

478

479 **Western Blot**

480 Cell extracts were collected in 100 mM Tris-HCl pH 8 with 1% SDS. Samples were
481 denatured in Laemmli buffer and heated at 95°C for 5 min. Total protein was resolved
482 on a 10% precast polyacrylamide gel (Bio-Rad) and transferred to a nitrocellulose
483 membrane for 75 min at 100 V. The membranes were blocked with Tris-buffered saline
484 with 0.1% Tween 20 (TBS-T) containing 5% skim milk, followed by incubation with
485 primary antibodies, overnight at 4°C. Membranes were washed and incubated with HRP-
486 conjugated secondary antibodies for 1 hour at room temperature and washed three times
487 before image acquisition. Images were acquired using Amersham ImageQuant™800
488 (Cytiva). Antibodies used: anti-Arpc5 (1:500 Santa Cruz Biotechnology, sc-166760);
489 anti-Arpc5L (1:500, Proteintech, 22025-1-AP); anti-Vinculin (1:1000, Sigma, V9131);
490 anti-rabbit HRP (1:5000, Thermo Scientific) and anti-mouse HRP (1:5000, Thermo
491 Scientific).

492

493 **Cryo-ET sample preparation**

494 GFP-Bin1 myoblasts were grown to approximately 60% confluency and then diluted to
495 a confluency of 10%. EM grids (Quantifoil R3.5/1 Au 200 mesh) were glow-discharged
496 using a plasma cleaner (PLASMAFLO PDC-FMG-2, Harrick Plasma) and then placed in
497 a 35mm MatTek dish in a flow hood. 300 µl of 5 µg/ml Fibronectin (Sigma-Aldrich,
498 341635) was added to the dish, covering the EM grids. The dish with the grids inside
499 was then sterilized under UV light for 1.5 hours. After simultaneous coating and
500 sterilization, the fibronectin was removed from the MatTek dish. The grids were then
501 washed twice with PBS and stored in approximately 300 µl of medium (DMEM high
502 glucose+Pyruvate+L-Glutamine; 10% FBS + 1% PenStrep).

503 Once the cells were ready, the medium in the grid-containing dish was removed, and
504 diluted cells were added to the dish. The cells were seeded on the EM grids at 37ºC 5%
505 CO_2 overnight (~15 hours). The following day, grids were inspected under an inverted
506 biological microscope (Medline Scientific™, 3650.0000) to check the cell density and
507 ensure grid integrity. Grids with minimally broken areas and well-distributed cells were
508 plunge frozen using Leica GP2 with back blotting for 15 seconds and an additional
509 movement of 0.5 mm at 37ºC and 90% humidity.

510

511

512

513 **Correlative light and electron microscopy**

514 Frozen grids were first loaded onto a Titan Krios microscope (Thermo Fisher Scientific)
515 operated at an accelerating voltage of 300 kV with a K3 detector and a BioQuantum
516 energy filter (Gatan). Grid atlas images were collected to check the ice quality and the
517 cell density using EPU software (Thermo Fisher Scientific). After locating the spread
518 cells, grids were transferred onto a cryo-light microscope (Leica THUNDER Imager EM
519 Cryo CLEM). Z stack fluorescence and bright field images were taken of the located
520 spread cells using LAS X software at 50X magnification. With the fluorescence images
521 processed using THUNDER technology, individual tubular fluorescence signals were
522 observed. The fluorescence images were saved for fluorescence microscopy (FM) and
523 electron microscopy (EM) image correlation. The grids were then transferred back to a
524 Titan Krios microscope (Thermo Fisher Scientific) operated at an accelerating voltage of
525 300 kV with Selectris X image filter (Thermo Fisher Scientific) and Falcon 4i camera
526 (Thermo Fisher Scientific). Medium magnification atlases were taken and combined on
527 each fluorescence-labelled cell for manual correlation and locating the regions of
528 interest. Empty holes and dark features were used as markers to facilitate the manual
529 correlation (Supplementary Figure 2B and 2C). After correlation, ROI with fluorescence
530 signals were targeted for cryo-ET tilt series data collection. 114 tilt series were collected
531 using TOMO5 software with a dose symmetric tilt scheme +/- 60° with the step size of
532 3° at the magnification of ×42,000, pixel size of 3.0 Å, dose rate of 12.6 e^-/pixel/s,
533 exposure time of 2.69s and total dose per micrograph of 3.66 e^-/ $Å^2$.

534

535 **Tomogram reconstruction**

536 Tomograms were reconstructed using RELION 4.1 tomography pipeline (Zivanov et al.,
537 2022). Raw data were imported into RELION followed by motion correction with
538 RELION's own implementation of MotionCor2 (Zheng et al., 2017) and CTF correction
539 with ctffind 4.1 (Rohou and Grigorieff, 2015). Tilt images with significant contamination
540 and grid bars were manually excluded from further data processing in a Napari-based
541 viewer (Exclude Tilt Images job). Then each tilt series was aligned using IMOD [CM4]
542 patch tracking with Patch size 100 nm and Patch overlap 50%. The aligned tilt series
543 were used to generate tomograms with a binned pixel size of 10 Å. Tomograms were
544 denoised using CryoCARE to improve the signal-to-noise level (Buchholz et al., 2019).
545 CryoCARE training was performed with 1200 sub-volumes per tomogram and a sub-
546 volume dimension of 72 pixel. Upon inspecting the tomograms, we found that 58

547 contained vesicular as opposed to tubular membrane structures (as shown in the
548 Supplementary Figure 2G) and were excluded. 23 of the tomograms were discarded due
549 to the presence by non-vitreous ice and could not be used for segmentation. Additionally,
550 27 tomograms did not correlate well with fluorescence signals because of the ambiguity
551 of fluorescence and the lack of correlation markers, which posed challenges for manual
552 correlation. 6 tomograms displayed tubular structures at locations where fluorescence
553 was observed. From these, the 3 highest quality tomograms were selected for
554 segmentation and further analysis.

555

556 **Tomogram Segmentation**

557 Tomograms were processed using IsoNet to further improve the signal-to-noise level
558 (Liu et al., 2022). The following parameters were used: CTD deconvolve snrfalloff of 0.5,
559 mask making density_percentage of 100, std_percentage of 100, and z_crop of 0.17.
560 Then, IsoNet-processed tomograms were cropped to remove regions lacking t-tubule
561 structures to simplify segmentation. Segmentation was performed using the neural
562 network-based software Dragonfly (Dragonfly 2024.1 [Computer software]. Comet
563 Technologies Canada Inc., Montreal, Canada; software available at
564 https://dragonfly.comet.tech/). For each tomogram, actin and membrane structures were
565 manually annotated on 5-12 sub-areas across different slices of the tomogram. The
566 segmented data were then used to train multiple deep-learning models. The model
567 segmenting the highest number of actin filaments on test slices was selected to segment
568 the entire tomogram. The UNet++ model (2.5D, 3 slices, depth level of 5, and initial filter
569 count of 32) was used for tomograms 1 and 2. Additionally, a pretrained UNet model
570 provided by the Dragonfly team (depth level of 5 and initial filter count of 64) was utilized
571 for tomogram 3. The segmentations were manually cleaned and corrected in Dragonfly.
572 The segmented actin and membrane structures were rendered into a 3D contour mesh
573 and smoothed over five to ten iterations for 3D visualization in Figure 3I and
574 Supplementary Figure 3. Movies were created by exporting the segmented actin and
575 membrane structures as binary files, converting these into two MRC files, and then
576 importing them along with a contrast-inverted 3D tomogram into ChimeraX for
577 visualization (Pettersen et al., 2021).

578

579

580

581 **Tomogram Analysis**

582 For tomogram analysis, sub-tomograms proximal to the t-tubules and distant from the t-
583 tubules were selected. The sub-volumes near t-tubules were constrained to regions no
584 more than 200 nm from the t-tubule structures. Actin branches – inferred from the relative
585 position of two connected filaments - within these boxes were identified, labelled, and
586 counted. For control purposes, sub-volumes located more than 200 nm away from t-
587 tubules were also identified, and suspected actin branches within these control sub-
588 volumes were similarly labelled and counted. In total, 7 sub-volumes were selected to
589 determine the number of actin branches near the t-tubules, and 3 sub-volumes were
590 selected as controls.

591

592 **Single-myofiber contraction and calcium transient assays**

593 In vitro myofibers were plated on 35mm fluorodishes (World Precision Instruments). After
594 7-8 days of differentiation, developed myofibers were imaged using a Nikon Eclipse Ti
595 microscope. Myofibers were kept at 37°C and CO_2 5% using an Okolab stage incubator
596 throughout all experimental procedures. Electrical field stimulation using the MyoPacer
597 system (Ionoptix) was used to induce excitation-contraction of myofibers using 10 Volts
598 at 0.5 Hz frequency pulses with a duration of 20 msec.

599 To measure cytosolic calcium transients during electrical pulses, myofibers at
600 differentiation day 3-4 were infected using 1 µl/ml of the AAV9-
601 pAAV.CAG.GCaMP6s.WPRE.SV40 (Addgene viral prep # 100844-AAV9; the plasmid
602 was a gift from Douglas Kim & GENIE Project (Chen et al., 2013)). After overnight
603 incubation, the media was replaced with differentiation media (IMDM with Glutamax
604 supplemented with 100 ng/ml recombinant agrin). After 7-8 days of differentiation,
605 GCaMP fluorescence during electrical field stimulation was recorded using a 60x Plan
606 Apo DM Ph3 (NA 1.4) objective, and an Andor Sona CSC-00324 camera at a 20 msec
607 frame rate with the NIS-Elements AR 5.42.05 software. Fiji software was then used to
608 generate subcellular GCaMP fluorescence kymographs by drawing a 475.7 μm^2 square
609 ROI along the myofiber that was then was maximum projected, generating GCaMP
610 fluorescence kymographs. The number of cells that presented GCaMP transients
611 synchronous with the electrical pulse was then quantified from these kymographs, and
612 plotted.

613 For single-myofiber contraction tracing, electrical field stimulation was performed as
614 mentioned above. Individual cell contractions were recorded with a MyoCam-S3™
615 camera (Ionoptix) and a 40x CFI Plan Apochromat Lambda D objective (NA 0.95), using

616 the IonWizard 7.7.3.180 software. Contraction kinetics were based on CytoMotion
617 (Ionoptix) Pixel Correlation changes relative to the reference frame taken at rest (i.e.
618 before electrical pulses). To generate single-myofiber contraction tracings, pixel
619 correlation (A.U.) curves were plotted using the Cytosolver Cloud (Ionoptix). Myofibers
620 that during the electrical stimuli did not contract, contract, present synchronous or
621 asynchronous contraction during the electrical stimulus were then quantified and plotted.

622

623 **Transmission Electron Microscopy (TEM) of *in vitro* myofibers**

624 Developed myofibers (7 days of differentiation) were fixed for 1 h at 4 °C in 0.1 M
625 Sorensen's Phosphate Buffer pH 7.4 containing 2.5% (v/v) glutaraldehyde (Science
626 Services EMS), 2% (v/v) formaldehyde (Science Services EMS) and 50 mM of calcium
627 chloride (Sigma). Samples were postfixed for 1 h at 4ºC in the dark with 0.1 M Sorensen's
628 Phosphate Buffer pH 7.4 containing 1% (w/v) osmium tetroxide (Science Services EMS)
629 and 0.8% (w/v) potassium ferrocyanide (Sigma-Aldrich). After five washes with distilled
630 water, samples were stained for 1h at room temperature with 0.5% (w/v) uranyl acetate
631 (Analar). Dehydration was performed using an ethanol gradient (30% 10 minutes room
632 temperature, 50% 10 minutes room temperature, 75% overnight 4ºC, 90% 10 minutes
633 room temperature, and 100% three times 10 minutes each room temperature). Samples
634 were embedded in Embed-812 epoxy resin (Science Services EMS) and hardened at
635 60 °C for at least 24 hours. Ultrathin sections (70 nm) were obtained and collected in
636 homemade formvar-carbon coated copper-palladium slot grids and counter-stained with
637 1% (w/v) uranyl acetate and Reynolds lead citrate, for 5 minutes each. Regions of
638 interest were mapped with SerialEM software and tiles of differentiated cells were
639 acquired using a FEI Tecnai G2 Spirit BioTWIN (120 kV) transmission electron
640 microscope with an Olympus-SIS Veleta CCD Camera.

641 Stitching was performed using the IMOD blendemont function (Kremer et al., 1996).
642 Stitched tiles were opened in Fiji and we counted the number of triads (one t-tubule
643 connected to two ER) in each tile, and normalized it to the cell area. To measure t-tubule
644 area, we identified the membrane objects that had a low electron-dense lumen, and that
645 were contacting the ER (green or blue arrowheads in Figure S4A). We then measured
646 its area by drawing a region of interest along the t-tubule membrane, using the drawing
647 tool from Fiji software.

648

649 **Data representation and statistics**

650 All graphs were generated and statistical analyses were conducted using GraphPad
651 Prism. Normality testing was carried out using the Shapiro-Wilk test, with an alpha
652 level=0.05. For normal distributions, t-student tests were performed. For datasets that
653 did not pass the normality test, statistical comparisons were performed using the Mann-
654 Whitney test. For paired samples that did not pass the normality test, the Wilcoxon test
655 was used. Statistical significance was defined as * $p<0.05$.

Acknowledgments

We thank all the members of the Gomes, Way and Moores laboratories for their continued support, scientific discussions and helpful comments on this work. We thank A.L. Sousa from the Electron Microscopy Facility at the Instituto Gulbenkian de Ciência for her technical expertise, sample processing, and imaging of differentiated myofibers by transmission electron microscopy (TEM). We also thank the Bioimaging Unit (funded by PPBI-POCI-01-0145-FEDER-022122) and the Rodent Facility of Instituto de Medicina Molecular João Lobo Antunes for their technical support. We thank N. Lukoyanova and S. Chen for electron microscope support and D. Houldershaw for computational support at Birkbeck.

Funding information

This work was supported by the European Research Council (ERC) under the European Union's Horizon 2020 research and innovation programme (grant agreement No 810207). Michael Way is additionally supported by the Francis Crick Institute, which receives its core funding from Cancer Research UK (CC2096), the UK Medical Research Council (CC2096), and the Wellcome Trust (CC2096). Ana Raquel Pereira was supported by the Fundação para a Ciência e Tecnologia (https://doi.org/10.54499/2022.07289.CEECIND/CP1727/CT0003). We acknowledge Diamond Light Source for access and support of the cryo-EM facilities at the UK's national Electron Bio-imaging Centre (eBIC) funder proposal EM20287-56, funded by the Wellcome Trust, MRC and BBSRC. Sample optimization and cryo-CLEM experiments were conducted in the ISMB EM facility (Birkbeck College, University of London) with financial support from the Wellcome Trust (202679/Z/16/Z, 206166/Z/17/Z) and UKRI-Medical Research Council (MR/X013359/1). For the purpose of Open Access, the authors have applied a CC BY public copyright licence to any Author Accepted Manuscript version arising from this submission.

Author contributions

A.R.P. and A.R.S. carried out experiments and analysed data. T.L., J.L.F. and C.A.M designed the cryo-CLEM experiments, T.L and J.L.F. performed collected the cryo-ET data, T.L. performed the 3D reconstruction and segmentation the experiments and, T.L and C.A.M analysed the data. G.L. performed the t-tubule cluster imaging. I.F. generated GFP-Bin1 lentivirus expressing plasmid. N.K. and M.W. provided unpublished data and tools. A.R.P, A.R.S, and E.R.G designed experiments and wrote the manuscript with assistance from other authors. All authors participated in the critical review and revision of the manuscript. E.R.G, M.W and C.A.M supervised the project and secured funding.

Declaration of Interest

The authors declare no competing interests.

References

Abella, J.V.G., Galloni, C., Pernier, J., Barry, D.J., Kjær, S., Carlier, M.-F., Way, M., 2016. Isoform diversity in the Arp2/3 complex determines actin filament dynamics. Nat. Cell Biol. 18, 76–86. https://doi.org/10.1038/ncb3286

Allard, A., Lopes dos Santos, R., Campillo, C., 2021. Remodelling of membrane tubules by the actin cytoskeleton. Biol. Cell 113, 329–343. https://doi.org/10.1111/boc.202000148

Al-Qusairi, L., Laporte, J., 2011. T-tubule biogenesis and triad formation in skeletal muscle and implication in human diseases. Skelet. Muscle 1, 26. https://doi.org/10.1186/2044-5040-1-26

Boncompagni, S., d'Amelio, L., Fulle, S., Fanò, G., Protasi, F., 2006. Progressive Disorganization of the Excitation–Contraction Coupling Apparatus in Aging Human Skeletal Muscle as Revealed by Electron Microscopy: A Possible Role in the Decline of Muscle Performance. J. Gerontol. Ser. A 61, 995–1008. https://doi.org/10.1093/gerona/61.10.995

Bovellan, M., Romeo, Y., Biro, M., Boden, A., Chugh, P., Yonis, A., Vaghela, M., Fritzsche, M., Moulding, D., Thorogate, R., Jégou, A., Thrasher, A.J., Romet-Lemonne, G., Roux, P.P., Paluch, E.K., Charras, G., 2014. Cellular control of cortical actin nucleation. Curr. Biol. CB 24, 1628–1635. https://doi.org/10.1016/j.cub.2014.05.069

Buchholz, T.-O., Krull, A., Shahidi, R., Pigino, G., Jékely, G., Jug, F., 2019. Content-aware image restoration for electron microscopy. Methods Cell Biol. 152, 277–289. https://doi.org/10.1016/bs.mcb.2019.05.001

Campbell-Valois, F.-X., Trost, M., Chemali, M., Dill, B.D., Laplante, A., Duclos, S., Sadeghi, S., Rondeau, C., Morrow, I.C., Bell, C., Gagnon, E., Hatsuzawa, K., Thibault, P., Desjardins, M., 2012. Quantitative proteomics reveals that only a subset of the endoplasmic reticulum contributes to the phagosome. Mol. Cell. Proteomics MCP 11, M111.016378. https://doi.org/10.1074/mcp.M111.016378

Campellone, K.G., Lebek, N.M., King, V.L., 2023. Branching out in different directions: Emerging cellular functions for the Arp2/3 complex and WASP-family actin nucleation factors. Eur. J. Cell Biol. 102, 151301. https://doi.org/10.1016/j.ejcb.2023.151301

Cao, L., Huang, S., Basant, A., Mladenov, M., Way, M., 2024. CK-666 and CK-869 differentially inhibit Arp2/3 iso-complexes. EMBO Rep. 1–19. https://doi.org/10.1038/s44319-024-00201-x

Chen, T.-W., Wardill, T.J., Sun, Y., Pulver, S.R., Renninger, S.L., Baohan, A., Schreiter, E.R., Kerr, R.A., Orger, M.B., Jayaraman, V., Looger, L.L., Svoboda, K., Kim, D.S., 2013. Ultrasensitive fluorescent proteins for imaging neuronal activity. Nature 499, 295–300. https://doi.org/10.1038/nature12354

Chertkova, A.O., Mastop, M., Postma, M., Van Bommel, N., Van Der Niet, S., Batenburg, K.L., Joosen, L., Gadella, T.W.J., Okada, Y., Goedhart, J., 2017. Robust and Bright Genetically Encoded Fluorescent Markers for Highlighting Structures and Compartments in Mammalian Cells. https://doi.org/10.1101/160374

Chugh, P., Paluch, E.K., 2018. The actin cortex at a glance. J. Cell Sci. 131, jcs186254. https://doi.org/10.1242/jcs.186254

Collins, A., Warrington, A., Taylor, K.A., Svitkina, T., 2011. Structural Organization of the Actin Cytoskeleton at Sites of Clathrin-Mediated Endocytosis. Curr. Biol. 21, 1167–1175. https://doi.org/10.1016/j.cub.2011.05.048

Di Ciano, C., Nie, Z., Szászi, K., Lewis, A., Uruno, T., Zhan, X., Rotstein, O.D., Mak, A., Kapus, A., 2002. Osmotic stress-induced remodeling of the cortical cytoskeleton. Am. J. Physiol. Cell Physiol. 283, C850-865. https://doi.org/10.1152/ajpcell.00018.2002

752 Dowling, J.J., Lawlor, M.W., Dirksen, R.T., 2014. Triadopathies: An Emerging Class of
753 Skeletal Muscle Diseases. Neurotherapeutics 11, 773–785.
754 https://doi.org/10.1007/s13311-014-0300-3
755 Ershov, D., Phan, M.-S., Pylvänäinen, J.W., Rigaud, S.U., Le Blanc, L., Charles-
756 Orszag, A., Conway, J.R.W., Laine, R.F., Roy, N.H., Bonazzi, D., Duménil, G.,
757 Jacquemet, G., Tinevez, J.-Y., 2022. TrackMate 7: integrating state-of-the-art
758 segmentation algorithms into tracking pipelines. Nat. Methods 19, 829–832.
759 https://doi.org/10.1038/s41592-022-01507-1
760 Falcone, S., Roman, W., Hnia, K., Gache, V., Didier, N., Lainé, J., Auradé, F., Marty, I.,
761 Nishino, I., Charlet-Berguerand, N., Romero, N.B., Marazzi, G., Sassoon, D.,
762 Laporte, J., Gomes, E.R., 2014. N-WASP is required for Amphiphysin-2/BIN1-
763 dependent nuclear positioning and triad organization in skeletal muscle and is
764 involved in the pathophysiology of centronuclear myopathy. EMBO Mol. Med. 6,
765 1455–1475. https://doi.org/10.15252/emmm.201404436
766 Fäßler, F., Javoor, M.G., Datler, J., Döring, H., Hofer, F.W., Dimchev, G., Hodirnau, V.-
767 V., Faix, J., Rottner, K., Schur, F.K.M., 2023. ArpC5 isoforms regulate Arp2/3
768 complex-dependent protrusion through differential Ena/VASP positioning. Sci.
769 Adv. 9, eadd6495. https://doi.org/10.1126/sciadv.add6495
770 Flucher, B.E., Takekura, H., Franzini-Armstrong, C., 1993. Development of the
771 excitation-contraction coupling apparatus in skeletal muscle: association of
772 sarcoplasmic reticulum and transverse tubules with myofibrils. Dev. Biol. 160,
773 135–147. https://doi.org/10.1006/dbio.1993.1292
774 Fourest-Lieuvin, A., Rendu, J., Osseni, A., Pernet-Gallay, K., Rossi, D., Oddoux, S.,
775 Brocard, J., Sorrentino, V., Marty, I., Fauré, J., 2012. Role of triadin in the
776 organization of reticulum membrane at the muscle triad. J. Cell Sci. 125, 3443–
777 3453. https://doi.org/10.1242/jcs.100958
778 Franzini-Armstrong, C., 2018. The relationship between form and function throughout
779 the history of excitation–contraction coupling. J. Gen. Physiol. 150, 189–210.
780 https://doi.org/10.1085/jgp.201711889
781 Galloni, C., Carra, D., Abella, J.V.G., Kjær, S., Singaravelu, P., Barry, D.J., Kogata, N.,
782 Guérin, C., Blanchoin, L., Way, M., 2021. MICAL2 enhances branched actin
783 network disassembly by oxidizing Arp3B-containing Arp2/3 complexes. J. Cell
784 Biol. 220, e202102043. https://doi.org/10.1083/jcb.202102043
785 Hall, T.E., Martel, N., Ariotti, N., Xiong, Z., Lo, H.P., Ferguson, C., Rae, J., Lim, Y.-W.,
786 Parton, R.G., 2020. In vivo cell biological screening identifies an endocytic
787 capture mechanism for T-tubule formation. Nat. Commun. 11, 3711.
788 https://doi.org/10.1038/s41467-020-17486-w
789 Janota, C.S., Pinto, A., Pezzarossa, A., Machado, P., Costa, J., Campinho, P., Franco,
790 C.A., Gomes, E.R., 2022. Shielding of actin by the endoplasmic reticulum
791 impacts nuclear positioning. Nat. Commun. 13, 2763.
792 https://doi.org/10.1038/s41467-022-30388-3
793 Kawaguchi, K., Fujita, N., 2024. Shaping transverse-tubules: central mechanisms that
794 play a role in the cytosol zoning for muscle contraction. J. Biochem. (Tokyo)
795 175, 125–131. https://doi.org/10.1093/jb/mvad083
796 Kosmalska, A.J., Casares, L., Elosegui-Artola, A., Thottacherry, J.J., Moreno-Vicente,
797 R., González-Tarragó, V., del Pozo, M.Á., Mayor, S., Arroyo, M., Navajas, D.,
798 Trepat, X., Gauthier, N.C., Roca-Cusachs, P., 2015. Physical principles of
799 membrane remodelling during cell mechanoadaptation. Nat. Commun. 6, 7292.
800 https://doi.org/10.1038/ncomms8292
801 Kremer, J.R., Mastronarde, D.N., McIntosh, J.R., 1996. Computer Visualization of
802 Three-Dimensional Image Data Using IMOD. J. Struct. Biol. 116, 71–76.
803 https://doi.org/10.1006/jsbi.1996.0013
804 Laplaud, V., Levernier, N., Pineau, J., Roman, M.S., Barbier, L., Sáez, P.J., Lennon-
805 Duménil, A.-M., Vargas, P., Kruse, K., du Roure, O., Piel, M., Heuvingh, J.,
806 2021. Pinching the cortex of live cells reveals thickness instabilities caused by

807 myosin II motors. Sci. Adv. 7, eabe3640.
808 https://doi.org/10.1126/sciadv.abe3640
809 Lee, C., Chen, L.B., 1988. Dynamic behavior of endoplasmic reticulum in living cells.
810 Cell 54, 37–46. https://doi.org/10.1016/0092-8674(88)90177-8
811 Lee, E., Marcucci, M., Daniell, L., Pypaert, M., Weisz, O.A., Ochoa, G.-C., Farsad, K.,
812 Wenk, M.R., De Camilli, P., 2002. Amphiphysin 2 (Bin1) and T-tubule
813 biogenesis in muscle. Science 297, 1193–1196.
814 https://doi.org/10.1126/science.1071362
815 Lemerle, E., Lainé, J., Benoist, M., Moulay, G., Bigot, A., Labasse, C., Madelaine, A.,
816 Canette, A., Aubin, P., Vallat, J.-M., Romero, N.B., Bitoun, M., Mouly, V., Marty,
817 I., Cadot, B., Picas, L., Vassilopoulos, S., 2023. Caveolae and Bin1 form ring-
818 shaped platforms for T-tubule initiation. eLife 12, e84139.
819 https://doi.org/10.7554/eLife.84139
820 Li, Y., Lipowsky, R., Dimova, R., 2011. Membrane nanotubes induced by aqueous
821 phase separation and stabilized by spontaneous curvature. Proc. Natl. Acad.
822 Sci. 108, 4731–4736. https://doi.org/10.1073/pnas.1015892108
823 Lionello, V.M., Kretz, C., Edelweiss, E., Crucifix, C., Gómez-Oca, R., Messaddeq, N.,
824 Buono, S., Koebel, P., Massana Muñoz, X., Diedhiou, N., Cowling, B.S., Bitoun,
825 M., Laporte, J., 2022. BIN1 modulation in vivo rescues dynamin-related
826 myopathy. Proc. Natl. Acad. Sci. 119, e2109576119.
827 https://doi.org/10.1073/pnas.2109576119
828 Liu, Y.-T., Zhang, H., Wang, H., Tao, C.-L., Bi, G.-Q., Zhou, Z.H., 2022. Isotropic
829 reconstruction for electron tomography with deep learning. Nat. Commun. 13,
830 6482. https://doi.org/10.1038/s41467-022-33957-8
831 Lo, H.P., Lim, Y.-W., Xiong, Z., Martel, N., Ferguson, C., Ariotti, N., Giacomotto, J.,
832 Rae, J., Floetenmeyer, M., Moradi, S.V., Gao, Y., Tillu, V.A., Xia, D., Wang, H.,
833 Rahnama, S., Nixon, S.J., Bastiani, M., Day, R.D., Smith, K.A., Palpant, N.J.,
834 Johnston, W.A., Alexandrov, K., Collins, B.M., Hall, T.E., Parton, R.G., 2021.
835 Cavin4 interacts with Bin1 to promote T-tubule formation and stability in
836 developing skeletal muscle. J. Cell Biol. 220, e201905065.
837 https://doi.org/10.1083/jcb.201905065
838 Nixon-Abell, J., Obara, C.J., Weigel, A.V., Li, D., Legant, W.R., Xu, C.S., Pasolli, H.A.,
839 Harvey, K., Hess, H.F., Betzig, E., Blackstone, C., Lippincott-Schwartz, J.,
840 2016. Increased spatiotemporal resolution reveals highly dynamic dense
841 tubular matrices in the peripheral ER. Science 354, aaf3928.
842 https://doi.org/10.1126/science.aaf3928
843 Peachey, L.D., 1965. THE SARCOPLASMIC RETICULUM AND TRANSVERSE
844 TUBULES OF THE FROG'S SARTORIUS. J. Cell Biol. 25, 209–231.
845 Pettersen, E.F., Goddard, T.D., Huang, C.C., Meng, E.C., Couch, G.S., Croll, T.I.,
846 Morris, J.H., Ferrin, T.E., 2021. UCSF ChimeraX: Structure visualization for
847 researchers, educators, and developers. Protein Sci. Publ. Protein Soc. 30, 70–
848 82. https://doi.org/10.1002/pro.3943
849 Picas, L., Viaud, J., Schauer, K., Vanni, S., Hnia, K., Fraisier, V., Roux, A., Bassereau,
850 P., Gaits-Iacovoni, F., Payrastre, B., Laporte, J., Manneville, J.-B., Goud, B.,
851 2014. BIN1/M-Amphiphysin2 induces clustering of phosphoinositides to recruit
852 its downstream partner dynamin. Nat. Commun. 5, 5647.
853 https://doi.org/10.1038/ncomms6647
854 Pimentel, M.R., Falcone, S., Cadot, B., Gomes, E.R., 2017. In Vitro Differentiation of
855 Mature Myofibers for Live Imaging. J. Vis. Exp. JoVE 55141.
856 https://doi.org/10.3791/55141
857 Pizarro-Cerdá, J., Chorev, D.S., Geiger, B., Cossart, P., 2017. The Diverse Family of
858 Arp2/3 Complexes. Trends Cell Biol. 27, 93–100.
859 https://doi.org/10.1016/j.tcb.2016.08.001
860 Porter, K.R., Palade, G.E., 1957. Studies on the endoplasmic reticulum. III. Its form
861 and distribution in striated muscle cells. J. Biophys. Biochem. Cytol. 3, 269–

300. https://doi.org/10.1083/jcb.3.2.269
Pylvänäinen, J.W., Laine, R.F., Saraiva, B.M.S., Ghimire, S., Follain, G., Henriques, R., Jacquemet, G., 2023. Fast4DReg – fast registration of 4D microscopy datasets. J. Cell Sci. 136, jcs260728. https://doi.org/10.1242/jcs.260728
Rohou, A., Grigorieff, N., 2015. CTFFIND4: Fast and accurate defocus estimation from electron micrographs. J. Struct. Biol. 192, 216–221. https://doi.org/10.1016/j.jsb.2015.08.008
Roman, W., Martins, J.P., Carvalho, F.A., Voituriez, R., Abella, J.V.G., Santos, N.C., Cadot, B., Way, M., Gomes, E.R., 2017. Myofibril contraction and cross-linking drive nuclear movement to the periphery of skeletal muscle. Nat. Cell Biol. 19, 1189–1201. https://doi.org/10.1038/ncb3605
Sadhu, L., Tsopoulidis, N., Hasanuzzaman, M., Laketa, V., Way, M., Fackler, O.T., 2023. ARPC5 isoforms and their regulation by calcium-calmodulin-N-WASP drive distinct Arp2/3-dependent actin remodeling events in CD4 T cells. eLife 12, e82450. https://doi.org/10.7554/eLife.82450
Schindelin, J., Arganda-Carreras, I., Frise, E., Kaynig, V., Longair, M., Pietzsch, T., Preibisch, S., Rueden, C., Saalfeld, S., Schmid, B., Tinevez, J.-Y., White, D.J., Hartenstein, V., Eliceiri, K., Tomancak, P., Cardona, A., 2012. Fiji: an open-source platform for biological-image analysis. Nat. Methods 9, 676–682. https://doi.org/10.1038/nmeth.2019
Sébastien, M., Aubin, P., Brocard, Jacques, Brocard, Julie, Marty, I., Fauré, J., 2020. Dynamics of triadin, a muscle-specific triad protein, within sarcoplasmic reticulum subdomains. Mol. Biol. Cell 31, 261–272. https://doi.org/10.1091/mbc.E19-07-0399
Serwas, D., Akamatsu, M., Moayed, A., Vegesna, K., Vasan, R., Hill, J.M., Schöneberg, J., Davies, K.M., Rangamani, P., Drubin, D.G., 2022. Mechanistic insights into actin force generation during vesicle formation from cryo-electron tomography. Dev. Cell 57, 1132-1145.e5. https://doi.org/10.1016/j.devcel.2022.04.012
Svitkina, T.M., 2020. Actin Cell Cortex: Structure and Molecular Organization. Trends Cell Biol. 30, 556–565. https://doi.org/10.1016/j.tcb.2020.03.005
Takekura, H., Flucher, B.E., Franzini-Armstrong, C., 2001. Sequential docking, molecular differentiation, and positioning of T-Tubule/SR junctions in developing mouse skeletal muscle. Dev. Biol. 239, 204–214. https://doi.org/10.1006/dbio.2001.0437
Várkuti, B.H., Képiró, M., Horváth, I.Á., Végner, L., Ráti, S., Zsigmond, Á., Hegyi, G., Lenkei, Z., Varga, M., Málnási-Csizmadia, A., 2016. A highly soluble, non-phototoxic, non-fluorescent blebbistatin derivative. Sci. Rep. 6, 26141. https://doi.org/10.1038/srep26141
Ward, S.R., Eng, C.M., Smallwood, L.H., Lieber, R.L., 2009. Are Current Measurements of Lower Extremity Muscle Architecture Accurate? Clin. Orthop. 467, 1074–1082. https://doi.org/10.1007/s11999-008-0594-8
Zheng, S.Q., Palovcak, E., Armache, J.-P., Verba, K.A., Cheng, Y., Agard, D.A., 2017. MotionCor2: anisotropic correction of beam-induced motion for improved cryo-electron microscopy. Nat. Methods 14, 331–332. https://doi.org/10.1038/nmeth.4193
Zivanov, J., Otón, J., Ke, Z., von Kügelgen, A., Pyle, E., Qu, K., Morado, D., Castaño-Díez, D., Zanetti, G., Bharat, T.A.M., Briggs, J.A.G., Scheres, S.H.W., 2022. A Bayesian approach to single-particle electron cryo-tomography in RELION-4.0. eLife 11, e83724. https://doi.org/10.7554/eLife.83724

Main Figures

Figure 1

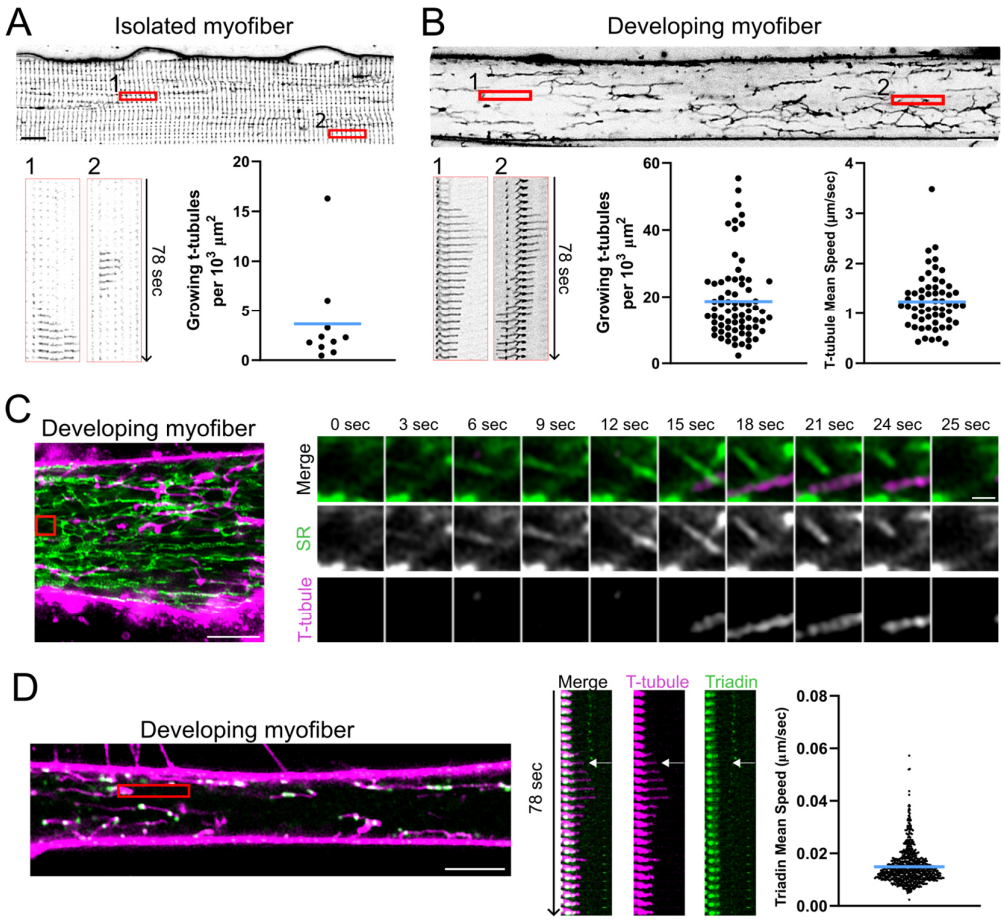

Figure 1 – T-tubules and ER are dynamic outside of the triad. (**A**) Top image corresponds to a timelapse snapshot of a matured isolated myofiber, stained with CellMask to label t-tubules and imaged by timelapse every 3 seconds for 2 minutes. Bottom image corresponds to kymographs from regions of interest (ROI) 1 and 2 of representative dynamic t-tubules. The plot represents the number of growing t-tubules per cell area during 2 minutes (N=9 isolated fibers, from three independent experiments). (**B**) Top image corresponds to a timelapse snapshot of an in vitro developing myofiber stained with CellMask to label t-tubules and imaged by timelapse every 3 seconds for 2 minutes. At this stage of development (differentiation day 4), t-tubules are starting to form and have a longitudinal orientation. Bottom image corresponds to kymographs from ROIs 1 and 2 of representative dynamic t-tubules. The plots represent the number of growing t-tubules per cell area during 2 min (N=72 cells, from three independent experiments) and t-tubule growth mean speed (N=58 growing t-tubules, from three independent experiments). (**C**) Left image corresponds to a timelapse snapshot of an in vitro developing myofiber (differentiation day 4) expressing GFP-KDEL (ER, green), stained with CellMask to label t-tubules (magenta) and imaged by timelapse every 3 seconds for 2 minutes. Right image corresponds to kymograph from red square ROI showing representative T-tubule and ER dynamics. (**D**) Left image corresponds to a timelapse snapshot of an in vitro developing myofiber (differentiation day 4) expressing Triadin-GFP (green), stained with CellMask (magenta) to label t-tubules and imaged by timelapse every 3 seconds for 2 minutes. Right image corresponds to kymograph from red ROI showing that Triadin-GFP is static when t-tubules are growing (white arrow). The plot represents Triadin-GFP mean speed in five different cells from two independent repeats (N=783). A-D scale bars 5 µm; C kymograph scale bar 0.5 µm. Blue lines on plots represent mean values.

940 **Figure 2**

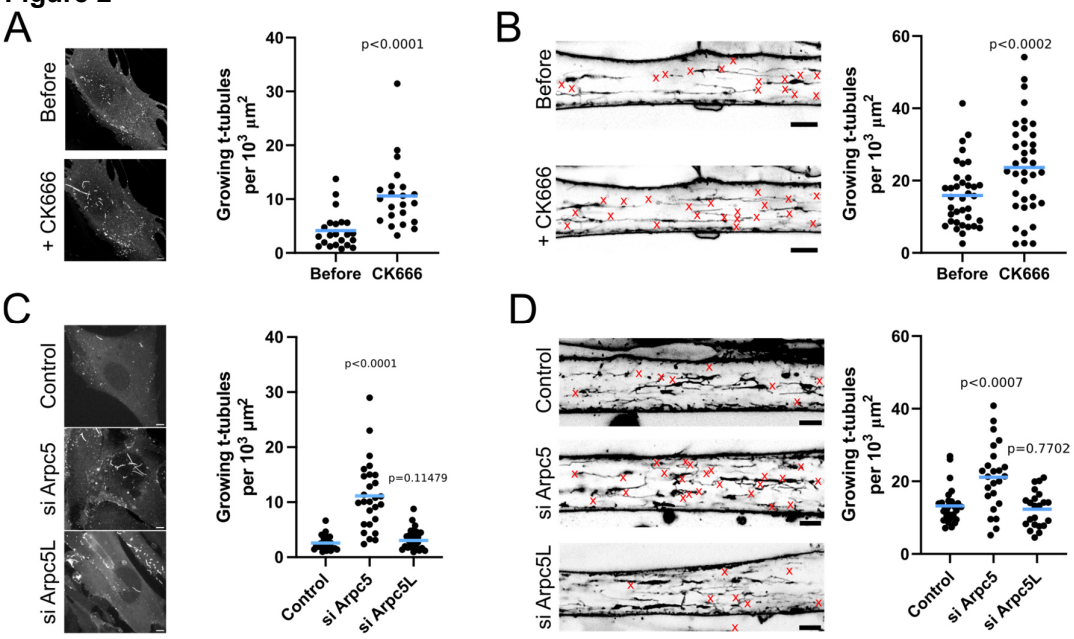

941

942 **Figure 2 – Inhibiting Arp2/3 with CK666 or through Arpc5 depletion promotes t-tubule**
943 **growth. (A)** Timelapse snapshots of GFP-Bin1 before or after CK666 addition. The plot
944 corresponds to the number of growing t-tubules per cell during 2 min before or after CK666
945 addition. Statistics: Wilcoxon test; N=22; results are from three independent experiments. **(B)**
946 Timelapse snapshots of in vitro developing myofibers (differentiation day 4) with CellMask labeled
947 t-tubules before or after CK666 addition. Red X indicates the site of t-tubule growth during 2 min.
948 The plot corresponds to the number of growing t-tubules per cell area during 2 min in the same
949 myofibers before or after CK666 addition. Statistics: Wilcoxon test; N=38 myofibers, results are
950 from three independent experiments. (**C**) Timelapse snapshots of GFP-Bin1 myoblasts
951 transfected with scramble (Control), Arpc5 (si Arpc5) or Arpc5L (si Arpc5L) siRNA. The plot
952 corresponds to the number of growing t-tubules per cell area during 2 min. Statistics: Mann-
953 Whitney; Control N=25; siArpC5 N=27; siArpC5L N=25. Results from three independent
954 experiments. (**D**) Timelapse snapshots of in vitro developing myofibers (differentiation day 4) with
955 CellMask-labelled t-tubules from scramble (Control); Arpc5 depleted (siArp5) or Arpc5L depleted
956 (siArpC5L) myofibers. Red X indicates sites of t-tubule growth during 2 min. The plot corresponds
957 to the number of growing t-tubules per cell area during 2 min. Statistics: Mann-Whitney; Control
958 N=29; siArpc5 N=24; siArpC5L N=22; results are from three independent experiments. Blue lines
959 on plots represent mean values. Scale bars 5 µm.

Figure 3

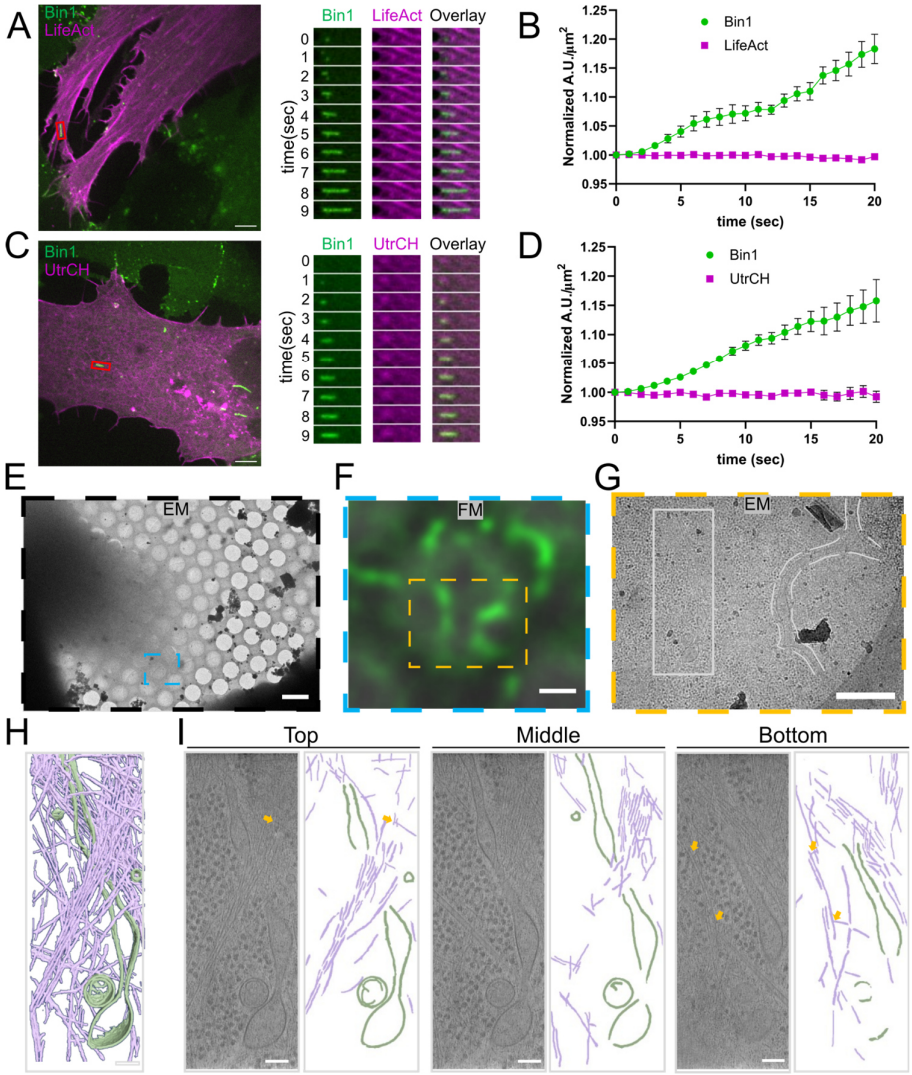

Figure 3 – F-actin is not locally nucleated at growing t-tubules. **(A)** Left image corresponds to a timelapse snapshot of GFP-Bin1 myoblasts (green) and LifeAct-mCherry (magenta). Right image corresponds to kymographs from the red rectangle ROI showing a t-tubule growing over time in the absence of F-actin changes. (**B**) Plots of LifeAct-mCherry and GFP-Bin1 average fluorescence intensity over time. Mean and SEM are represented. N=19 from two independent experiments. (**C**) Left image corresponds to a timelapse snapshot of GFP-Bin1 myoblasts (green) and mScarlet-I-UtrCH (magenta). Right image corresponds to kymographs from the red rectangle ROI showing a t-tubule growing over time in the absence of F-actin changes. (**D**) Plots of the mScarlet-I-UtrCH and GFP-Bin1 average fluorescence intensity over time. Mean and SEM are represented. N=16 from two independent experiments. (**E**) Representative low magnification cryo-EM image showing part of one cell on a TEM grid. The cyan rectangle indicates the ROI imaged using epifluorescence and brightfield microscopy (panel F). (**F**) Merged epifluorescence (green) and brightfield (grey, FM) image of the ROI. in E, showing multiple GFP-Bin1 t-tubules at the cell periphery. The orange rectangle indicates the ROI imaged using TEM (panel G). (**G**) Medium magnification TEM image of the ROI in F, showing the t-tubules observed in F. (**H**) 3D representation of cropped tomogram segmentation of the white rectangle ROI from G, with actin filaments (purple) and t-tubule membrane (green). (**I**) Slices of the tomogram in H at different z positions (from left to right: z=-25nm, 30nm and 135nm relative to the central slice) with actin filaments (purple), t-tubule membrane (green), and potential actin branches (yellow arrows). Scale bar: 5 µm in A, B and E, 1 µm in F, 500 nm in G and 100 nm in H and I.

982 **Figure 4**

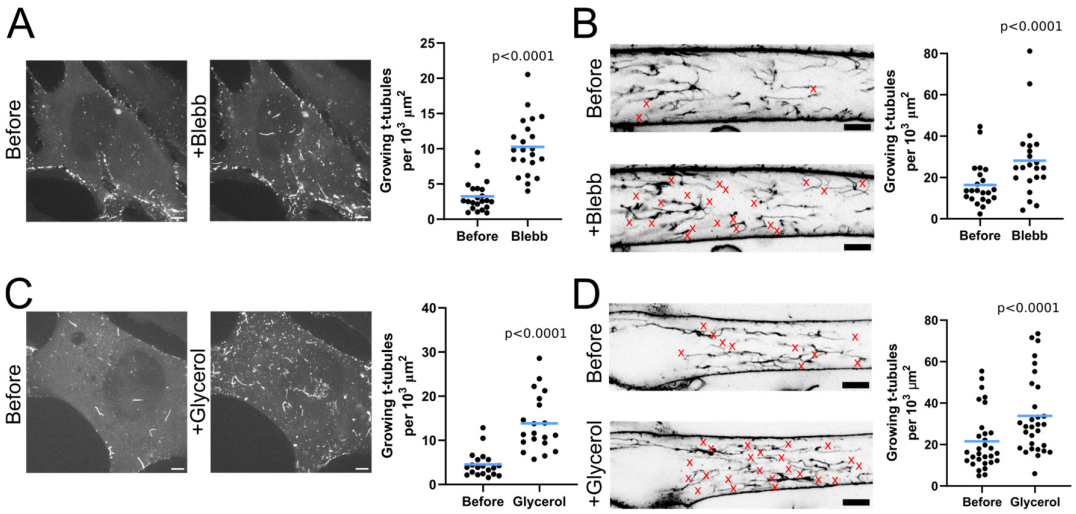

983

984 **Figure 4 – Cortical actin disruption promotes t-tubule growth**. (**A**) Timelapse snapshots of
985 GFP-Bin1 myoblasts before or after para-aminoblebbistatin addition (Blebb). The plot
986 corresponds to the number of growing t-tubules per cell area for 2 min before or after para-
987 aminoblebbistatin addition. Statistics: Wilcoxon test; N=22 cells, results are from three
988 independent experiments. (**B**) Timelapse snapshots of in vitro developing myofibers
989 (differentiation day 4) with CellMask labeled t-tubules before or after para-aminoblebbistatin
990 addition (Blebb). Red X indicates the site of t-tubule growth during 2 min. The plot corresponds
991 to the number of growing t-tubules per cell area during 2 min in the same myofibers before or
992 after para-aminoblebbistatin addition. Statistics: Wilcoxon test; N=31 myofibers, results are from
993 three independent experiments. (**C**) Timelapse snapshots of GFP-Bin1 myoblasts before or after
994 glycerol addition. The plot corresponds to the number of growing t-tubules per cell area for 2 min
995 before or after glycerol addition. Statistics: Wilcoxon test; N=20 cells, results are from three
996 independent experiments. (**D**) Timelapse snapshots of in vitro developing myofibers
997 (differentiation day 4) with CellMask labeled t-tubules before or after glycerol addition. Red X
998 indicates the site of t-tubule growth during 2 min. The plot corresponds to the number of growing
999 t-tubules per cell area during 2 min in the same myofibers before or after glycerol addition.
1000 Statistics: Wilcoxon test; N=20 myofibers, results are from three independent experiments. Scale
1001 bars 5 µm. Blue lines on plots represent mean value.

1002

1003 **Figure 5**

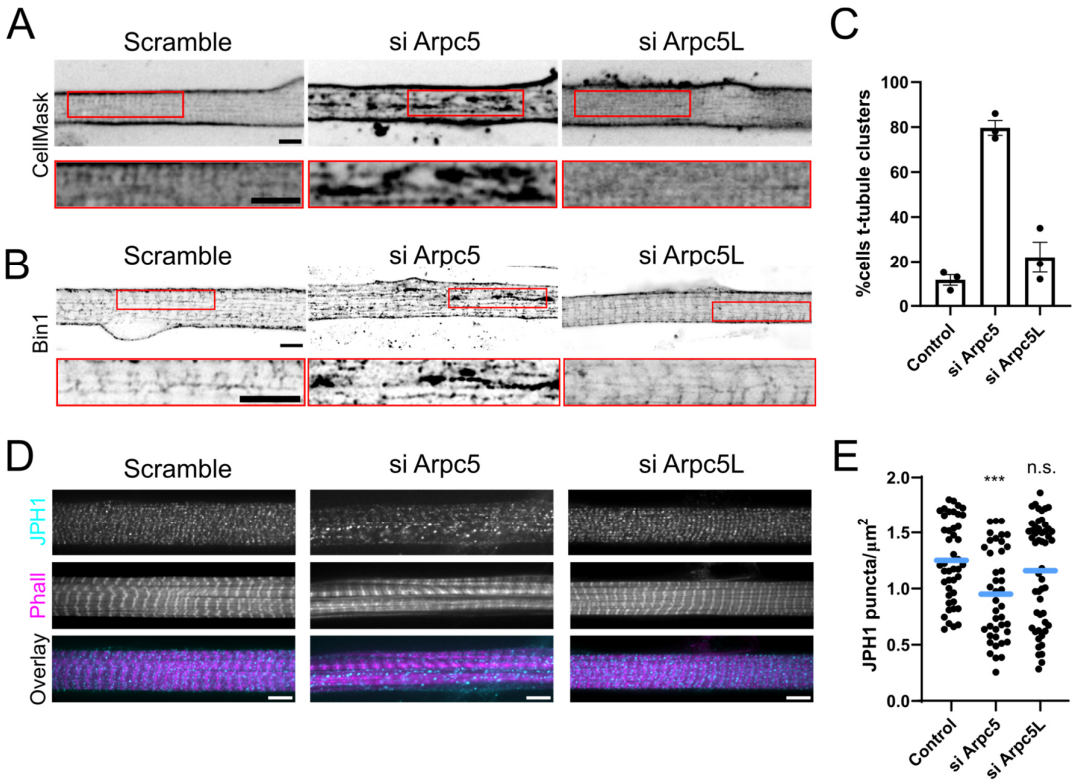

1004

1005 **Figure 5 – Arpc5 depletion leads to t-tubule clusters and reduction Junctophilin1 puncta**
1006 **in differentiated myofibers. (A)** Representative images of CellMask labelled t-tubules from
1007 control (scramble), Arpc5 (si Arpc5), or Arpc5L (si Arpc5L) depleted myofibers (differentiation day
1008 7). Magnifications corresponding to the red boxes are shown below each image. **(B)**
1009 Representative images of Bin1 immunostained t-tubules from control (scramble), Arpc5 (si
1010 Arpc5), or Arpc5L (siArpc5L) depleted myofibers (differentiation day 7). Magnifications
1011 corresponding to the red boxes are shown below each image. (**C**) Quantification of the
1012 percentage of myofibers with t-tubule clusters.Control N=42 myofibers; si Arpc5 N= 41 myofibers;
1013 si Arpc5L N=50 myofibers, from two independent experiments. (**D**) Representative images of
1014 control (scramble), Arpc5 (si Arpc5), or Arpc5L (siArpc5L) depleted myofibers (differentiation day
1015 7) immunostained for Junctophilin 1 (JPH1, cyan), Bin1 (Yellow); and stained with phalloidin
1016 (Phall, magenta). (**E**) Quantification of the number of Junctophilin 1 (JPH1) puncta per μm^2 in
1017 scramble (Control); Arpc5 (si Arpc5) or in Arpc5L depleted myofibers (si Arpc5L). Statistics:
1018 Mann-Whitney statistical test, siArpc5 P-value = 0,0005; siArpc5L P-value = 0,3161; Control N=44
1019 myofibers; si Arpc5 N=41 myofibers; si Arpc5L N=51 myofibers. Results are from three
1020 independent experiments. Scale bars 5 µm. Blue lines on plots represent mean values.
1021

1022 **Figure 6**

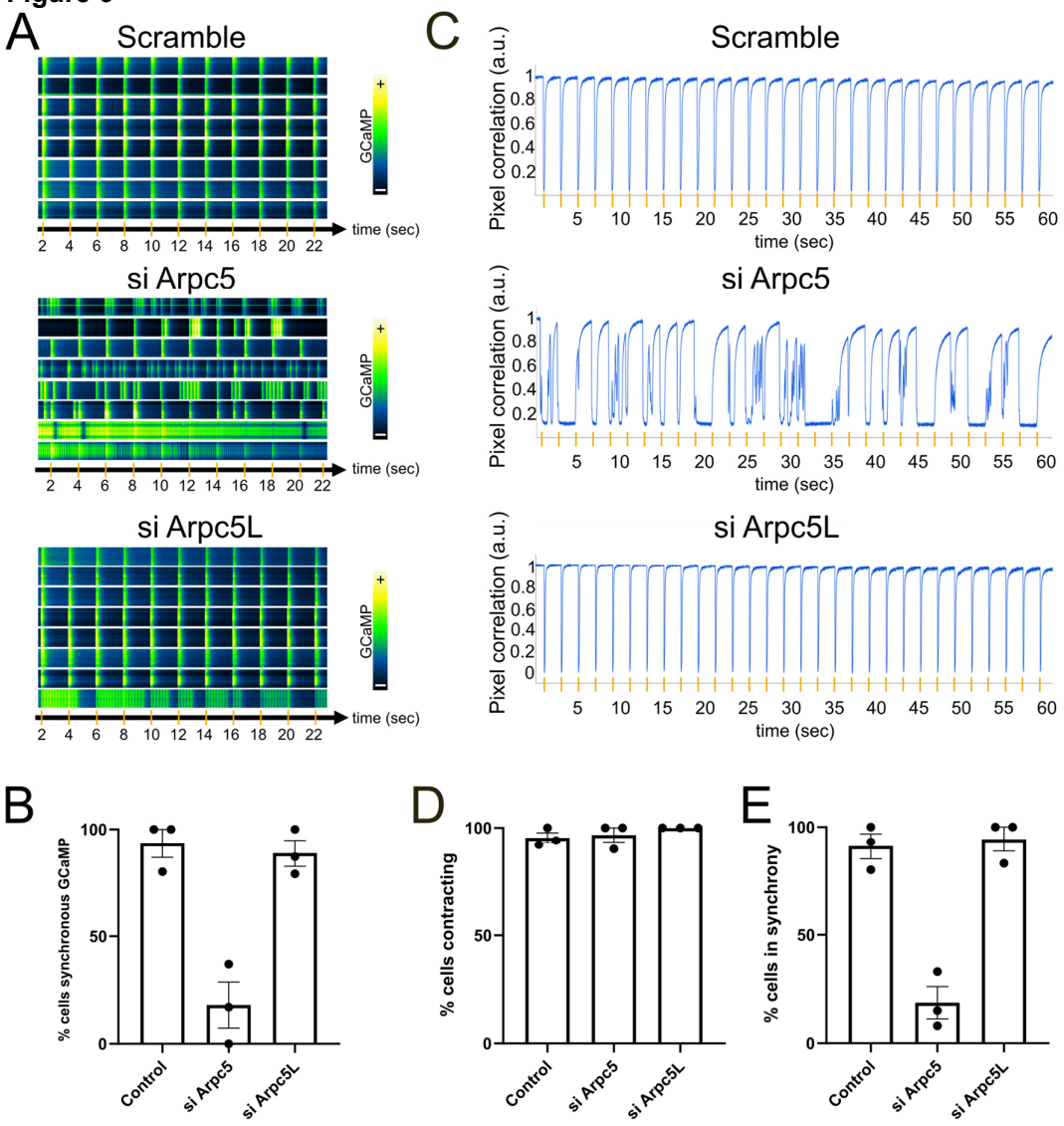

1023
1024
1025 **Figure 6 – Arpc5 depletion leads to asynchronous muscle contraction (A)** Myofibers
1026 (differentiation day 7-8) expressing GCaMP were stimulated with 10 V at a frequency of 0.5 Hz
1027 and subcellular GCaMP fluorescence kymographs from 8 different myofibers of control
1028 (Scramble), Arpc5 (siArpc5) and Arpc5L (si Arpc5L) are shown. Orange marks indicate electrical
1029 pulses. (**B**) Quantification of the percentage of myofibers from A with GCaMP fluorescence
1030 transients synchronised with the electrical pulse. Control N=40, si Arpc5 N=62, si Arpc5L N=52.
1031 Results are from three independent experiments. (**C**) Representative contraction tracing
1032 recordings from control (Scramble), Arpc5 (si Arpc5), and Arpc5L (si Arpc5L) depleted myofiber.
1033 Orange marks indicate electrical pulses. (**D**) Quantification of the percentage of contracting
1034 myofibers from C. Control N=43, siArpc5 N=36, siArpc5L N=28. Results are from three
1035 independent experiments. (**E**) Quantification of the percentage of myofibers from **C** that contract
1036 in synchrony with the electrical impulse. Control N=41, siArpc5 N=35, siArpc5L N=28. Results
1037 are from three independent experiments.

1038 **Supplementary Figures**

1039

1040 **Figure S1**

1041

A

B

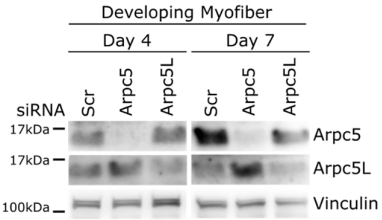

1042

1043

1044 **Figure S1 - Arpc5 and Arpc5L depletion . Related to Figure 2.** (**A**) Western blots of GFP-Bin1
1045 myoblasts knocked down for scramble (Scr) Arpc5 or Arpc5L isoforms. Membranes were blotted
1046 using antibodies against Arpc5 or Arpc5L with vinculin as a loading control. (**B**) Western blots of
1047 myofibers (differentiation day 4 or day 7), knocked down for scramble (Scr), Arpc5 or Arpc5L.
1048 Membranes were blotted using antibodies against Arpc5 and Arpc5L isoforms and vinculin, used
1049 as a loading control.

1050

1051 **Figure S2**

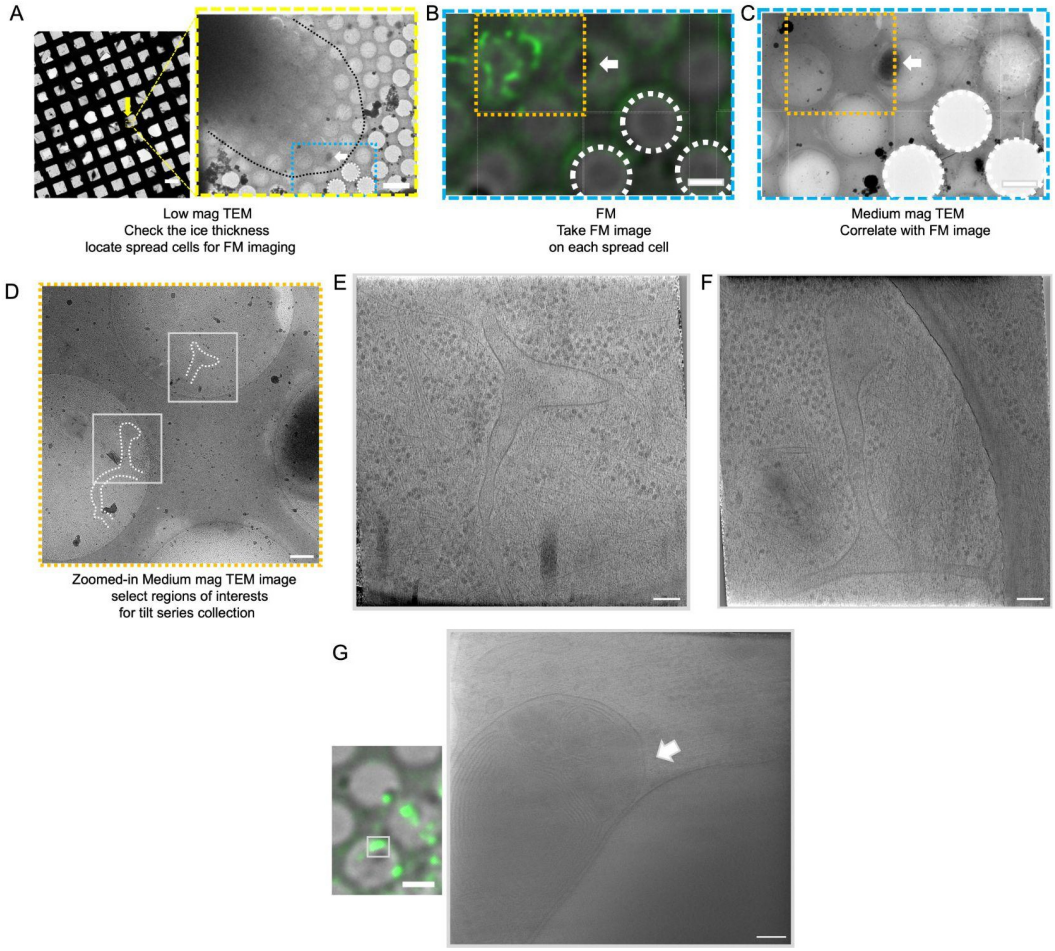

1052
1053
1054 **Figure S2 - Correlative light and electron microscopy workflow. Related to Figure3.**
1055 (**A**) Cells were imaged using TEM to check the ice thickness and locate spread cells for FM
1056 imaging. In the example image, one spread cell is indicated with a yellow arrow, with the
1057 approximate cell periphery outlined in black in the zoomed view. (**B**) Cells imaged using cryo-
1058 fluorescence microscopy (FM) with the bright-field image of the area in the blue box from A
1059 showing the GFP-Bin1-labeled t-tubule structures at the cell periphery. (**C**) Cells were re-imaged
1060 using medium magnification TEM images in tiles and combined for FM-TEM correlation. The
1061 empty holes and black features were used for manual correlation, with empty holes indicated by
1062 white circles and the dark feature marked by a white arrow. (**D**) A zoomed-in view of the medium
1063 mag image collected from the orange region in C. Tubular membrane structures are highlighted
1064 with white curvy lines. The shapes of these tubular membrane structures resemble those seen in
1065 the FM image in B. Regions of interest (ROI) were selected for tilt series data collection, indicated
1066 by white boxes. (**E**) and (**F**) The central slice along the z-axis of the 3D tomogram at positions 1
1067 and 2, respectively. (**G**) The bright-field and FM image showing fluorescently-labelled vesicular
1068 structure. A tomographic slice of the reconstruction inside the white box showing nested sets of
1069 membranes is shown on the right. Scale bar: 100 µm and 5 µm in A, 2 µm in B and C,500 nm in
1070 D, 100 nm in E and F. 2 µm and 100 nm in G.

Figure S3

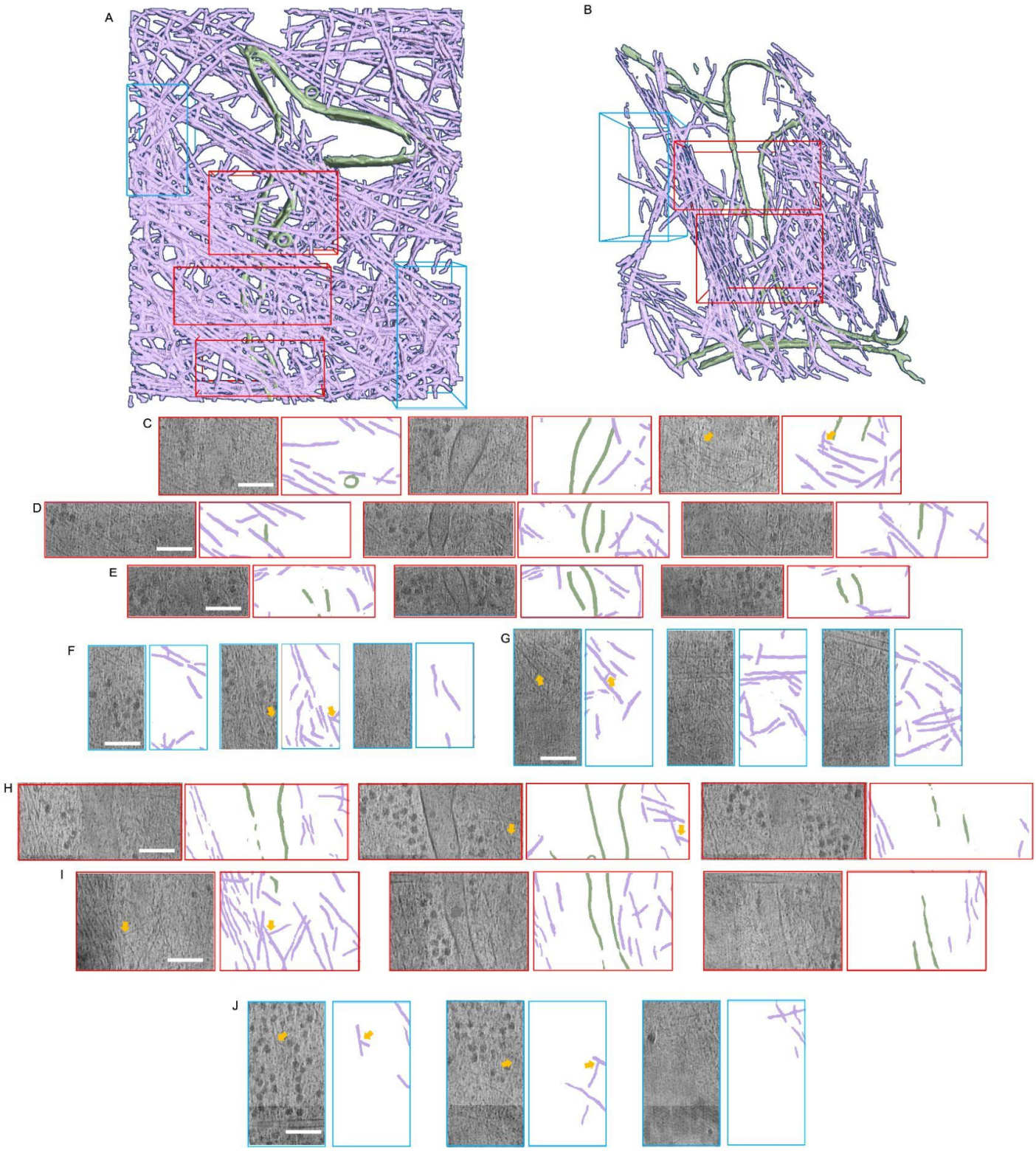

Figure S3 - Quantitative analysis of cryo-electron tomograms. Related to Figure 3. (**A**) 3D representation of cropped tomogram segmentation in Supplementary Fig1E, sub-volumes proximal to and distant from T-tubule membrane used for counting branch number indicated with red boxes and blue boxes, respectively. (**B**) 3D representation of cropped tomogram

segmentation in Supplementary Fig1F, sub-volumes proximal to and distant from T-tubule membrane used for counting branch number indicated with red boxes and blue boxes, respectively. (**C**) Slices and segmentations of the tomogram in A in red box1 at different z positions (from left to right: z=-35nm, 5nm and 34nm relative to the central slice) with actin filaments in purple, T-tubules in green, and potential actin branches indicated with yellow arrows. Scale bar: 100 nm. (**D**) Slices and segmentations of the tomogram in A in red box2 at different z positions (from left to right: z=-26nm, 3nm and 28nm relative to the central slice) with actin filaments in purple, T-tubules in green.Scale bar: 100 nm. (**E**) Slices and segmentations of the tomogram in A in red box3 at different z positions (from left to right: z=1 nm, 14 nm and 34nm relative to the central slice) with actin filaments in purple, T-tubules in green.Scale bar: 100 nm. (**F**) Slices and segmentations of the tomogram in in A blue box1 at different z positions (from left to right: z=-27 nm, 3 nm and 22 nm relative to the central slice) with actin filaments in purple, T-tubules in green, and potential actin branches indicated with yellow arrows. Scale bar: 100 nm. (**G**) Slices and segmentations of the tomogram in A in blue box2 at different z positions (from left to right: z=-13nm, 10nm and 31nm relative to the central slice) with actin filaments in purple, T-tubules in green, and potential actin branches indicated with yellow arrows. Scale bar: 100 nm. (**H**) Slices and segmentations of the tomogram in B in red box1 at different z positions (from left to right: z=-15nm, 11nm and 34nm relative to the central slice) with actin filaments in purple, T-tubules in green, and potential actin branches indicated with yellow arrows. Scale bar: 100 nm. (**I**) Slices and segmentations of the tomogram in B in red box2 at different z positions (from left to right: z=-22 nm, 7 nm and 30 nm relative to the central slice) with actin filaments in purple, T-tubules in green, and potential actin branches indicated with yellow arrows. Scale bar: 100 nm. (**J**) Slices and segmentations of the tomogram in B in blue box at different z positions (from left to right: z=-14 nm, 16 nm and 39 nm relative to the central slice) with actin filaments in purple, T-tubules in green, and potential actin branches indicated with yellow arrows. Scale bar: 100 nm.

Figure S4

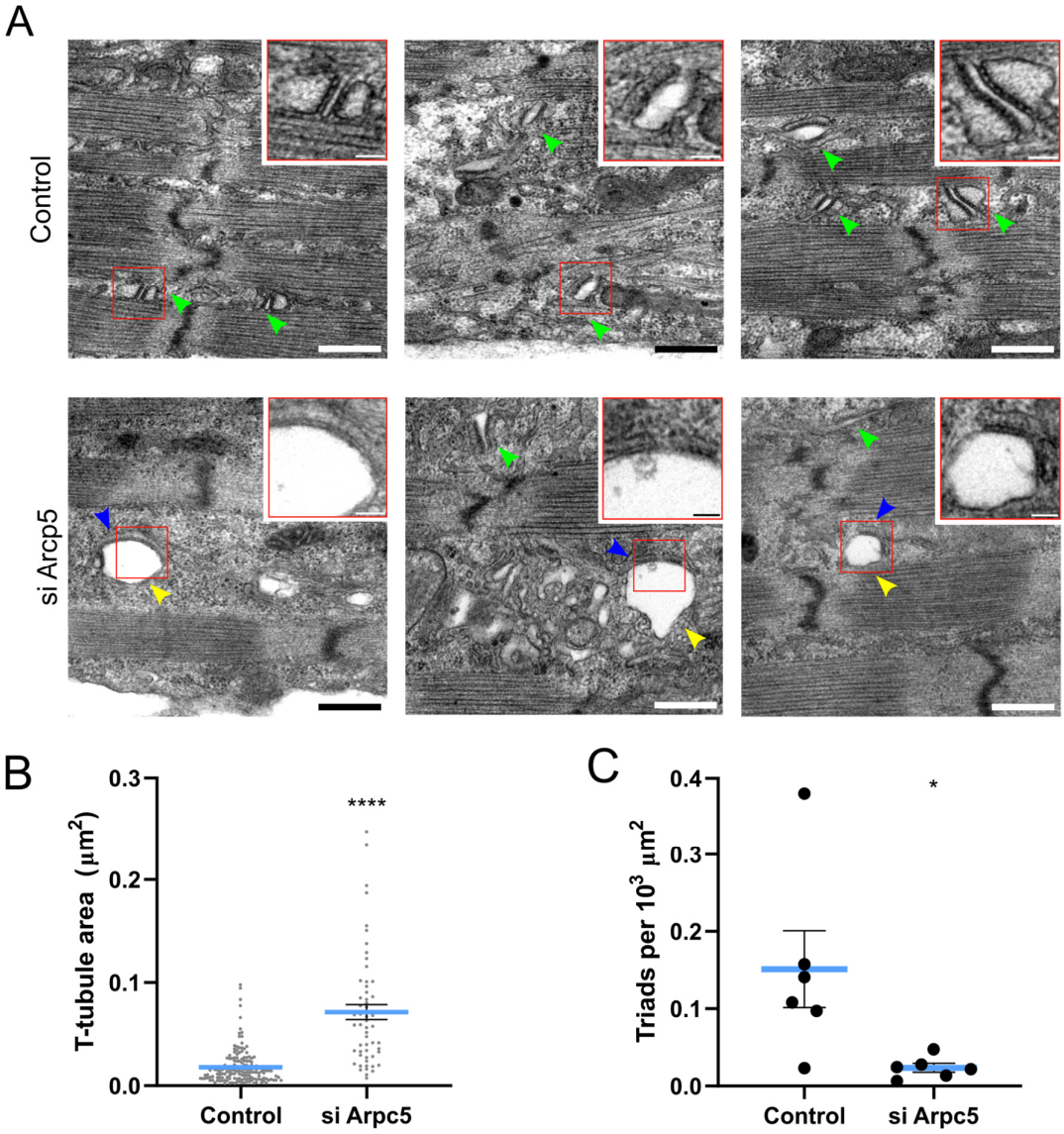

Figure S4 – Transmission Electron Microscopy (TEM) of stained and resin-embedded myofibers. Related to Figure 5. (**A**) TEM of scramble (Control) or Arpc5 (si Arpc5) depleted myofibers (differentiation day 7). Green arrowheads indicate triads (one t-tubule in contact with two adjacent ER compartments). Blue arrows indicate t-tubules connected to the ER only on one side, not forming a triad. Yellow arrowheads indicate enlarged t-tubules. Scale bars 500 nm. Magnifications corresponding to the red ROIs are shown as insets, Scale bars 100 nm. (**B**) Plot representing the area of each t-tubule observed in cells from A. Control N=162 t-tubules, si Arpc5 N=56 t-tubules. A total of 6 cells were quantified per condition, two biological replicates. Mann-Whitney test ($p<0.0001$). (**C**) Quantifications of the number of triads normalized for cell area (10^3 μm^2). t-test ($p=0.0286$) Blue lines in graphs represent mean values. Black lines in graphs represent SEM.

Video legends

Video S1 – Timelapse movie of t-tubule dynamics in a myofiber isolated from the EDL muscle of an adult mice. Isolated fiber was stained with CellMask to label t-tubules. Scale bar 5 µm. Related to Figure 1.

Video S2 – Timelapse movie of t-tubule dynamics in a developing in vitro myofiber. Cells were stained with CellMask to label t-tubules. Scale bar 5 µm. Related to Figure 1.

Video S3 – Timelapse movie of Endoplasmic Reticulum (GFP-KDEL, green) and t-tubule (CellMask, magenta) dynamics in a developing myofiber. Scale bar 5 µm. Related to Figure 1.

Video S4 – Timelapse movie of Triadin (green) and t-tubule (magenta) dynamics in a developing in vitro myofiber. Cells expressing Triadin-GFP stained with CellMask to label t-tubules. Scale bar 5 µm. Related to Figure 1.

Video S5 – Timelapse movie of t-tubule dynamics in GFP-Bin1 myoblasts before CK666. Scale bar 5 µm. Related to Figure 2.

Video S6 – Timelapse movie of t-tubule dynamics in GFP-Bin1 myoblasts after CK666. Scale bar 5 µm. Related to Figure 2.

Video S7 – Timelapse movie of t-tubule dynamics in a developing myofiber before adding CK666. Cells were stained with CellMask to label t-tubules. Scale bar 5 µm. Related to Figure 2.

Video S8 – Timelapse movie of t-tubule dynamics in a developing myofiber after a 5 minute incubation with CK666. Scale bar 5 µm. Related to Figure 2.

Video S9 – Timelapse movie of t-tubule dynamics in GFP-Bin1 myoblasts depleted for scramble control. Scale bar 5 µm. Related to Figure 2.

Video S10 – Timelapse movie of t-tubule dynamics in GFP-Bin1 depleted for Arpc5. Scale bar 5 µm. Related to Figure 2.

Video S11 – Timelapse movie of t-tubule dynamics in GFP-Bin1 myoblasts depleted for Arpc5L. Scale bar 5 µm. Related to Figure 2.

Video S12 – Timelapse movie of t-tubule dynamics in a developing myofiber in scramble cells (Control). T-tubules were stained with CellMask. Scale bar 5 µm. Related to Figure 2.

Video S13 – Timelapse movie of t-tubule dynamics in a developing myofiber depleted for Arpc5. Scale bar 5 µm. Related to Figure 2.

Video S14 – Timelapse movie of t-tubule dynamics in a developing myofiber depleted for Arpc5L. Scale bar 5 µm. Related to Figure 2.

Video S15 – F-actin (LifeAct-mCherry, magenta) and t-tubules (Bin1-GFP, green) in GFP-Bin1 myoblasts. Scale bar 5 µm. Related to Figure 3.

Video S16 – F-actin (mScarlet-i-UtrCH, magenta) and t-tubules (Bin1-GFP, green) in GFP-Bin1 myoblasts. Scale bar 5 µm. Related to Figure 3.

Video S17 – Cryo-electron tomogram and segmentation model of actin cytoskeleton around t-tubule site related to Figure 3I. Actin cytoskeleton coloured in light purple. T-tubule membrane coloured in green.

Video S18 – Cryo-electron tomogram and segmentation model of actin cytoskeleton around t-tubule site related to Figure S3A. Actin cytoskeleton coloured in light purple. T-tubule membrane coloured in green.

Video S19 – Cryo-electron tomogram and segmentation model of actin cytoskeleton around t-tubule site related to Figure S3B. Actin cytoskeleton coloured in light purple. T-tubule membrane coloured in green.

Video S20 – Timelapse movie of t-tubule dynamics in GFP-Bin1 myoblasts before para-aminoblebbistatin (Blebb). Scale Bar 5 µm. Related to Figure 4.

Video S21 – Timelapse movie of t-tubule dynamics in GFP-Bin1 myoblasts after para-aminoblebbistatin (Blebb). Scale Bar 5 µm. Related to Figure 4.

Video S22 – Timelapse movie of t-tubule dynamics in a developing in vitro myofiber before adding para-aminoblebbistatin. Cells were stained with CellMask to label t-tubules. Scale bar 5 µm. Related to Figure 4.

Video S23 – Timelapse movie of t-tubule dynamics in a developing in vitro myofiber after a 5 minute incubation with para-aminoblebbistatin. Scale bar 5 µm. Related to Figure 4.

Video S24 - Timelapse movie of t-tubule dynamics in GFP-Bin1 myoblasts before glycerol. Scale Bar 5 µm. Related to Figure 4.

Video S25 - Timelapse movie of t-tubule dynamics in GFP-Bin1 myoblasts after glycerol. Scale Bar 5 µm. Related to Figure 4.

Video S26 - Timelapse movie of t-tubule dynamics in a developing myofiber before glycerol. Cells were stained with CellMask to label t-tubules. Scale bar 5 µm. Related to Figure 4.

Video S27 - Timelapse movie of t-tubule dynamics in a developing in vitro myofiber after glycerol. Cells were stained with CellMask to label t-tubules. Scale bar 5 µm. Related to Figure 4.